Universität Zürich[UZH]

Simon Buse

Dark Matter Electron Scattering with Xurich II

Master Thesis

Experimental Particle Physics

The Faculty of Science (MNF)
University of Zurich

Supervision

Prof. Dr. Laura Baudis
Dr. Patricia Sanchez-Lucas

September 2021

Abstract

In this thesis the hypothetical interactions of sub-GeV dark matter particles with electrons was studied with data from a small dual-phase xenon time projection chamber operated at the Earth's surface. Considered was the scattering both on electrons and nuclei in the Earth's crust, atmosphere, and shielding materials to compute the attenuation of the dark matter flux by the atmosphere and the overburden. Based on an ionisation-only event selection and an exposure of $\sim 15\,\mathrm{g}\,\mathrm{days}$ with no background subtraction, the data was evaluated in terms of various models, including interactions mediated by a heavy and ultralight dark photon as well as through an electric dipole moment. For the case of a heavy dark photon mediator, new parameter space for dark matter particle masses in the range $100 - 400\,\mathrm{MeV}$ is excluded.

Contents

Introduction

This document describes the master project that was conducted in the experimental particle physics group of Prof. Laura Baudis at the University of Zurich (UZH) in the fall semester of 2020 and in the spring semester of 2021.

The main subject of the thesis, a small liquid xenon dual-phase time projection chamber (TPC) called Xurich II, was developed, built and improved over several years starting from 2011. In recent years the TPC was equipped with a new array of photosensors and used to study new calibration sources at low energies. In this thesis, background data from a calibration run in 2019 is used to study light dark matter models that detectors on the surface of the Earth have increased sensitivity to. The stopping power of shielding material reduces the dark matter flux and limits the sensitivity of underground experiments towards dark matter that scatters repeatedly. The attenuation of the dark matter flux is included in the models by the use of a recently published Monte Carlo tool, that fully simulates the scattering in the overburden, for example in the shielding material.

The motivation for the search of light dark matter comes from the absence of a WIMP signal, the most promising dark matter candidate in recent years, and the lack of a full description of events with only a ionization signal in dual-phase xenon TPCs. Theses signals, where only a few electrons are produced, are quite abundant and could arise from interactions of light dark matter with atomic electrons. The signals where studied and compared to three different dark matter models, two assume an interaction that is mediated by a massive dark photon and one assumes a coupling to the electric dipole moment. For two models the emerging constraints coincide with previous constraints from other experiments and for one model new constraints where found.

The thesis is organized into 7 chapters. The first two chapters are an introduction to the dark matter problem and the search technique using dual-phase TPCs. In chapter 3, the specific light dark matter model is described before in chapter 4 the backgrounds in the region of interest and general limitations of TPCs are discussed. In chapter 5 the main data analysis follows, which starts with the basic signal properties and then moves on to find all the events that are compatible with the dark matter signal structure. In chapter 6, the detection capabilities of Xurich II are estimated with data-driven approaches and in the last chapter, the derived model constraints are presented and discussed.

Chapter 1

Dark Matter

Conceptually, the problem of dark matter is very similar to the old problem of unseen planets. By observing astrophysical systems some anomalies appear and theories explain them either by assuming the existence of a large amount of unseen mass or by assuming deviations from the known laws of gravity. History showed that both solutions can be accurate and both have solved the problem already once. In the case of the orbital motion anomalies of Uranus, the postulation of an unseen mass within the solar system lead to the discovery of Neptune. And in the case of Mercury's precession anomaly, Einstein's General relativity theory was required to correctly describe the orbit.

The issue today is that Einstein's field equations and the ordinary visible amount of matter in the universe are not sufficient to describe a whole collection of astrophysical and cosmological observations. Similar to the case of Uranus, multiple observations could be explained by proposing a large amount of matter that has not been observed yet. This theory introduces what is referred to as *dark matter* and is by far the most accepted solution to the problem. In the following, a few astrophysical and cosmological observations will be discussed that hint towards additional mass or changes in the laws of gravity.

1.1 Evidence

Galaxy clusters

In 1933, galaxy clusters provided some of the first evidence for dark matter. Back then Fritz Zwicky studied the Coma Cluster and determined that there is not enough visible matter to explain the velocity dispersion of galaxies in the cluster. He proposed that there is 400 times more dark mass than visible mass, which is a lot more than is accepted today [1].

Collisions of clusters are especially puzzling study objects because the visible matter and the gravitationally interacting matter are observed to be separated. The electromagnetically interacting gas, which makes up the most part of the ordinary matter, is slowed down during the collision while the stars of the galaxies bypass each other almost undisturbed. Observations through X-rays and gravitational lensing show the displacement between the visible mass and the gravitationally interacting mass. This displacement shows that there is a mass component that interacts only very weakly with the ordinary matter but appears

through its gravitational effect. In the left panel of figure 1.1 the famous example of the galaxy cluster 1E 0657-56, also known as the "bullet cluster", is shown.

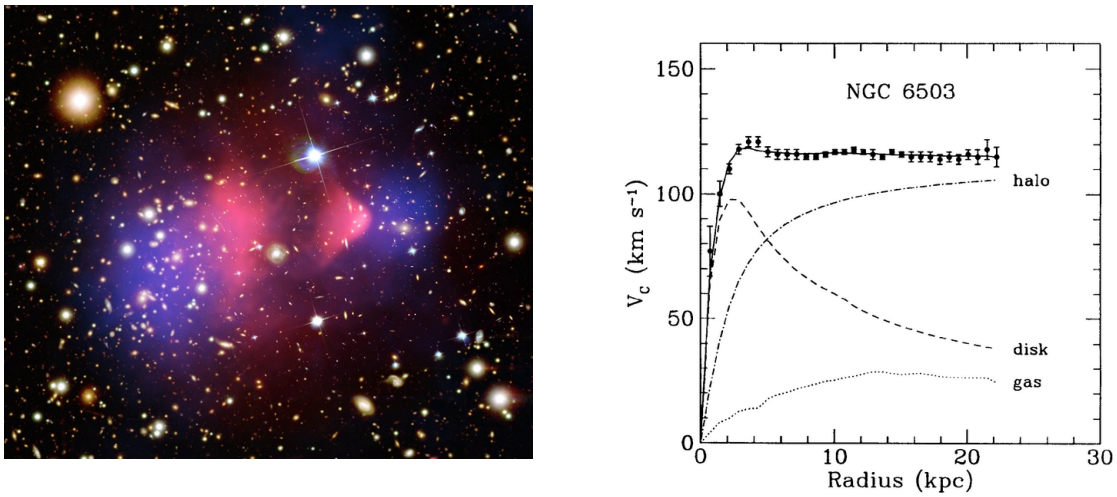

Figure 1.1: Right: A composite image shows the observed offsets of the mass distribution by gravitational lensing (blue) from the distribution of the dominant visible mass inferred by X-rays (pink). The displacement directly demonstrates the presence and dominance of dark matter in this cluster [2]. Left: The measured rotation curve of NGC 6503 is shown together with the individual rotation curves of gas, disk and halo that could explain the data. The figure is taken from [3].

Rotational velocities in galaxies

In the 1970s more evidence for additional mass in galaxies was found by Vera Rubin et al. [4]. When the orbital speeds of visible stars or gas in a disc galaxy is plotted against the radial distance from that galaxy's center, the expected $v \sim 1/\sqrt{r}$ relation was not observed. This is predicted by the observed mass distribution and the equality of the gravitational and centrifugal force. Instead, flat rotation curves were observed which can be explained by more undetected mass in the system. In the right panel of figure 1.1 an example of a flat rotation curves is shown and in chapter 3 the mass distribution that could cause such a curve will be discussed.

Structure formations

Without dark matter, the universe would not have the observed structure on large scales. Dark matter does not experience radiation pressure and therefore clumps more efficiently and in turn, forces the normal matter to form more dense structures as well. Simulations with no dark matter are not able to reproduce the observed large-scale structures and point to the existence of non-relativistic dark matter [5].

Cosmic microwave background

The balance between gravity and pressure in the early universe has left its signatures in the cosmic microwave background (CMB), the faint leftover radiation from the time when the early universe cooled enough to become transparent. The photons that existed since

the so-called *last scattering* have been propagating ever since, becoming fainter and less energetic, due to the redshift caused by the expansion of the universe. The CMB is one of the pillars of the hot Big Bang model of cosmology and was measured by various satellites with the most precise measurement coming from the Planck satellite [6]. The CMB exhibits an almost perfect black body spectrum with a temperature of 2.725 K and has a tiny anisotropy, meaning the temperature is not perfectly homogeneous measured in all directions. In the left panel of figure 1.2 the temperature difference over the whole sky-map is shown after all the known microwave sources like dust or individual sources from the Milky Way were subtracted.

The anisotropy contains the gravitational imprints of dark matter and provides some of the strongest evidence for the ΛCDM-model, often referred to as the *standard model of cosmology*. The ΛCDM very successfully explains the anisotropies with a linear combination of spherical harmonics and states that the ordinary (baryonic) matter makes up only 15% of the matter in the universe and the missing 85% consists of cold dark matter. In the right panel of figure 1.2 the temperature fluctuations as a function of the angular scale, the distance in the sky-map, and as a function of the multipole moment l, is shown. In these power spectra, the ratio of the second and third peaks show the presence of dark matter.

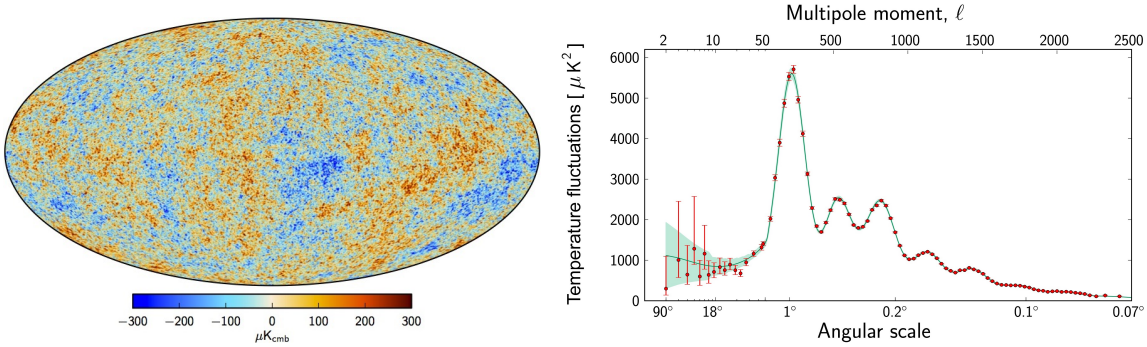

Figure 1.2: Left: CMB intensity map at 5' resolution derived from the joint baseline analysis of Planck, WMAP, and 408 MHz observations. Figure form [7]. Right: Temperature fluctuation as function of the angular size and the multipole moment l, measured by the Planck experiment (red points) and with the best-fit from the ΛCDM model (light green line). For comparison, the diameter of the full Moon in the sky is about half a degree. Figure from [8].

1.2 Properties

The postulated dark matter has quite peculiar properties. It does for example neither emit, absorb, nor reflect light at any frequency. This non-interacting property represented with the adjective *dark* would maybe better be described with the term *transparent* matter. Moreover, it is assumed that dark matter interacts gravitationally and the energy density falls off inversely with the volume. The large-scale behavior of dark matter is generally much better understood than its microscopic properties. Dark matter seems to accumulate around galaxies, clusters of galaxies, and form halos instead of being homogeneously spread through space. These properties rule out all of the known particles in the Standard Model

of particle physics. Even though the neutrinos have very similar properties, they would be a candidate for what is called *hot dark matter*. This means that dark matter would be moving at a velocity comparable to the speed of light but this kind of behavior is ruled out by many different arguments. The observed structure formation in the early universe, for instance, would not have been possible with only hot dark matter. Dark matter therefore must be cold which is to say non-relativistic at the time of decoupling [1].

1.3 Detection Techniques

In general, there are three ideas to detect dark matter via interactions with constituents of the Standard Model. They can intuitively be displayed in a Feynman-like diagram, see figure 1.3.

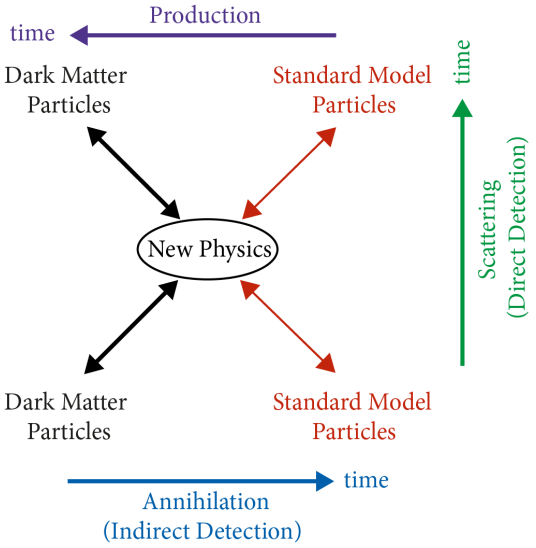

Figure 1.3: Possible detection channels of dark matter interacting with particles from the Standard Model. Dark matter can either be detected by production at particle colliders, indirectly by self-annihilation products, or by the scattering of Standard Model particles.

Production: If dark matter or the mediator between the dark sector and components of the Standard Model, is light enough it could in principle be produced at the Large Hadron Collider (LHC) at CERN. One particular type of search, so-called "mono-X" searches, look for missing transverse momentum together with a mono-object (a photon, a single jet, a Z, etc) [9, 10]. Since dark matter needs to be stable it can account for the missing momentum and thereby indicate its presence. However so far no collider search has found any convincing dark matter signal [11].

Indirect detection: The dark matter annihilation into standard model particles could lead to potential signatures in the CMB and other astrophysical observables such as X-rays, gamma rays, antiprotons, positrons or neutrinos. Indirect searches are looking for an anomalous flux in any of these observables coming from places where dark matter has gravitationally accumulated like galaxies, the Sun or the Earth. Detecting the different

[1] The abbreviation CDM in ΛCDM stands for *cold dark matter* and expresses exactly this feature.

signatures requires very different detectors like Cherenkov telescopes (HESS [12], CTA [13]), neutrino detectors (Super-Kamiokande [14], IceCube [15]) or detector on satellites (Fermi-LAT [16]). This method relies heavily on the dark matter density, astrophysical uncertainties, and background sources. No convincing signal of dark matter has yet been confirmed through indirect searches [17].

Direct detection: In an interaction between dark matter and ordinary matter kinetic energy is transferred to either the atomic nuclei or atomic electrons and the recoil energy could be detected. Various experimental techniques and target materials are being used for these searches and depending on the specific dark matter interaction different experiments yield the best results. This technique requires very detailed knowledge about background sources that create similar signals and enormous efforts are put into the reduction of these backgrounds. A particle interaction can be detected through three different channels: phonons (heat), charge (ionisation) or light (scintillation). In figure 1.4 an overview over the different detection channels and their respective experiments is shown.

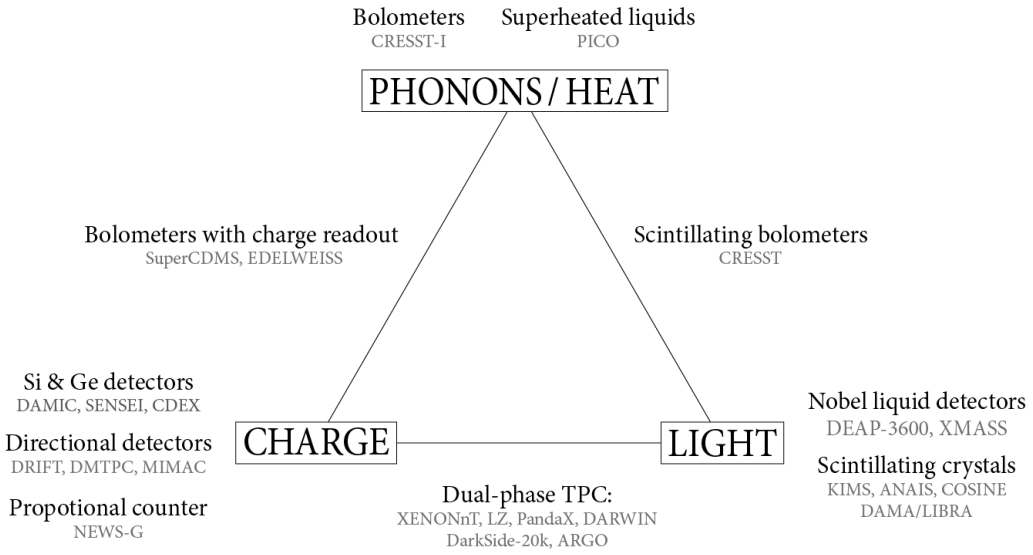

Figure 1.4: Shown are the single particle excitation detection channels that are used in direct detection searches together with example experiments for each detection technique. This is by no means a complete list of all the experiments nor of all the detection techniques.

1.4 Candidates

Most direct detection efforts where in recent years directed towards the detection of the so-called *weakly interacting massive particles* (WIMPs) or *axions*. WIMPs are conjectured to be relatively heavy $\mathcal{O}(\mathrm{GeV} - \mathrm{TeV})$ where axions are predicted to be very light $\mathcal{O}(\mathrm{peV} - \mathrm{meV})$. Both particle classes emerge from theoretical extensions of the Standard Model. Axions would provide a solution to the strong CP problem, that describes the lack of an explanation for the CP conservation in quantum chromodynamics. A solution for this problem was derived in 1977 by Peccei and Quinn that introduced a new symmetry and a light pseudoscalar particle called axion [18, 19]. WIMPs on the other hand are introduced

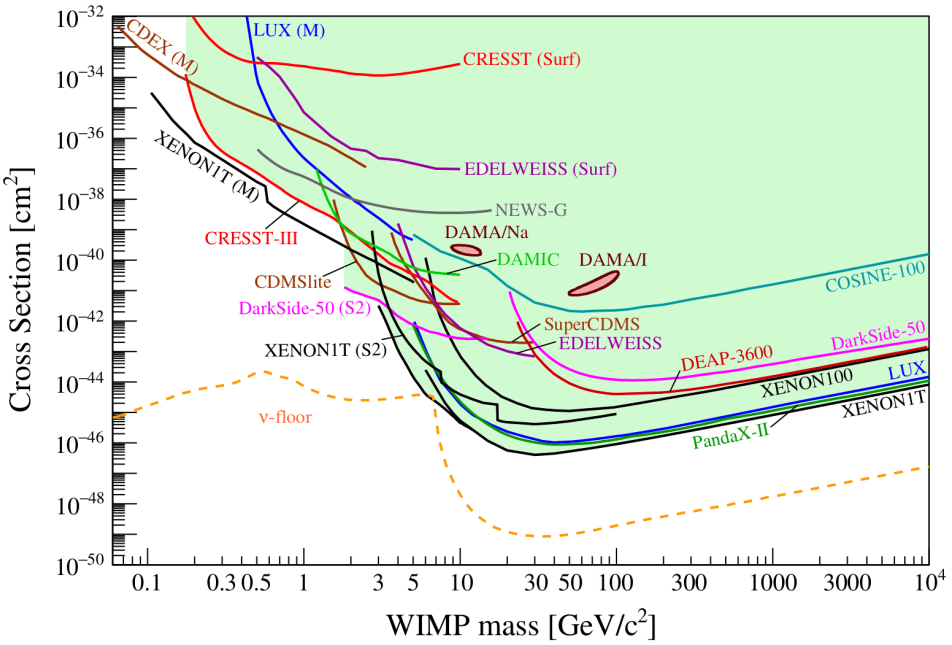

Figure 1.5: Current status of searches for spin-independent elastic WIMP-nucleus scattering assuming the standard parameters for an isothermal WIMP halo: $\rho_0 = 0.3$ GeV/cm3, $v_0 = 220$ km/s, $v_{esc} = 544$ km/ s. Results labelled "M" were obtained assuming the Migdal effect. Results labelled "Surf" are from experiments not operated underground. The figure and the caption are taken from [26].

in many Standard Model extensions, for example in supersymmetric theories [20]. Additional motivation for WIMPs comes from what has been called the *WIMP-miracle*. If a new stable particle existed in the mentioned mass range, and if it interacted with Standard Model particles via a force at the electroweak scale, then the dark matter density that is observed today could have been produced by thermal freeze-out in the early universe. This surprising coincidence has further motivated the search during the last decades [20].

Due to the different predicted masses, the two candidate classes are thought to be detectable by utilizing different detection techniques. Axions require experiments looking for the *wave-like* properties of the candidates while WIMPs are searched for assuming *particle-like* properties. In figure 1.5 the most stringent limits for spin-independent WIMP-nucleon interaction are shown. As visible, a large parameter space is already excluded and the current strongest exclusion bounds are derived from large dual-phase xenon TPCs (XENON1T [21], LUX [22], PandaX-II [23]) and are followed closely by argon single and dual-phase experiments (DEAP-3600 [24], Dark-Side 50 [25]) .

1.5 Light Dark Matter Searches

As there has not been any trace of WIMPs, alternative explanations are becoming more popular. Especially, the search of lighter dark matter (often called sub-GeV dark matter) has received some attention in the last few years. The introduction to the specific dark matter model that is searched for in this thesis will follow in chapter 3 but now the motivation and basic detection principle shall be discussed.

A experimental difficulty that arises when dark matter is very light resides in its kinetic energy, described by the dark matter halo velocity distribution. The kinetic energy $\approx m_\chi v^2$ resembles the maximal energy that can be passed to the target material and is related to the dark matter mass m_χ by a factor 10^{-6}, assuming a typical velocity of 10^{-3} (in units of c) from a Maxwell-Boltzmann halo distribution. This implies for a WIMP with mass 1 GeV a recoil energy of a bout 1 keV, which is close to the detection threshold for experiments looking for nuclear recoils. Thus the created signal can quickly fall below the detection threshold when dark matter is lighter. The fact that nuclear recoil experiments are limited towards light dark matter is visible in the rise of the exclusion bounds towards lighter mass in figure 1.5 and implies the need of a different detection mechanism for the search of lighter dark matter particles.

An alternative for many experiments is to look for dark matter-electron interactions instead and use the fact that electrons are much lighter than nuclei. If an electron receives enough energy in a scattering event they can easily be ionized from an atom (binding energy $\mathcal{O}(10\,eV)$) or promoted to the conduction band in a semiconductor (binding energy $\mathcal{O}(1\,eV)$). If experiments are sensitive to such signals, dedicates searches for this interactions can be performed. In figure 1.6 the current best exclusion bounds for dark matter electron scattering are shown. It has to be emphasised that the exclusion bounds are the result of separate searches, which have to be distinguished from the exclusion bounds in figure 1.5. The strongest limits for this type of interaction come from either silicon based experiments (SENSEI [27], DAMIC [28]) or from dual-phase xenon TPCs (XENON1T [29], XENON10 [30, 31]).

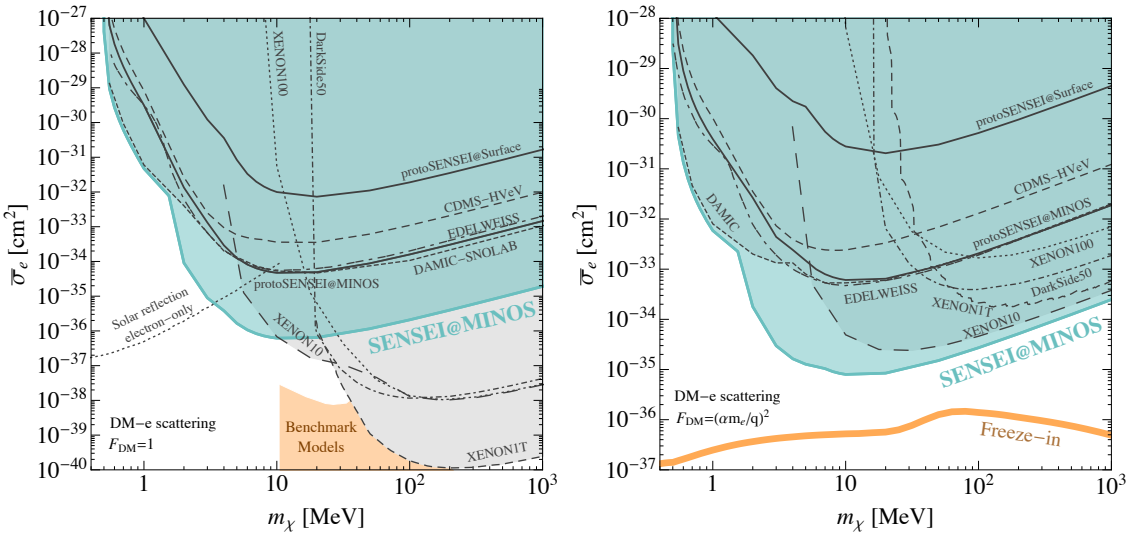

Figure 1.6: 90% confidence level constraints (grey and cyan shaded regions) on the dark matter electron scattering cross section are shown for two different mediators: a heavy mediator (left) and an ultralight mediator (right). See chapter 3 for more explanations on the dark matter electron interaction model and its parametrization. The figure is taken from [27].

The above exclusion bounds show the limits towards weak interactions, where dark matter would create only very rarely a signal, up to the point where the signal happens so rarely that they become indistinguishable from backgrounds. Such models can not be constrained because experiments are simply not sensitive enough to probe them and consequently some parameter space remains unprobed. Next to this reasoning there is another possibility that could explain why experiments have not found dark matter yet: namely the possibility that dark matter does not reach the detector because it interacts *strongly* [2], meaning with a interaction cross section around 1 barn [3], and is stopped before it reaches the detector. Strongly interacting dark matter is not a new idea and the first direct detection experiments were conducted in 1987 [32]. The difference nowadays is that the search has expanded towards lighter mass and here the idea of strongly interaction dark matter is being reconsidered via dark matter electron interactions [33].

The dark matter electron scattering rate was first worked out in 2012 [34] and evaluated for data of the XENON10 experiment [30]. The model does not only include a new dark matter particle but also a new mediator. A detailed model description will follow in chapter 4. The new force carrier creates a new degree of freedom and a large variety of interactions can be studied [35]. The sensitivity of current experiments towards such interactions and the limitations due to scattering in the overburden have been studied in [33]. In figure 1.7 the exclusion bounds (red region) for a ultralight mediator are shown. Here the upper boundary includes scattering in material above the detector like the atmosphere, the Earth's crust or the shielding material.

[2] *Strongly* reefers only to the strength of the interaction between the Standard Model and the dark sector and does not mean an interaction mediated by the strong force of Quantum Chromodynamics (QCD).

[3] 1 barn = $10^{-24}\,cm^2$

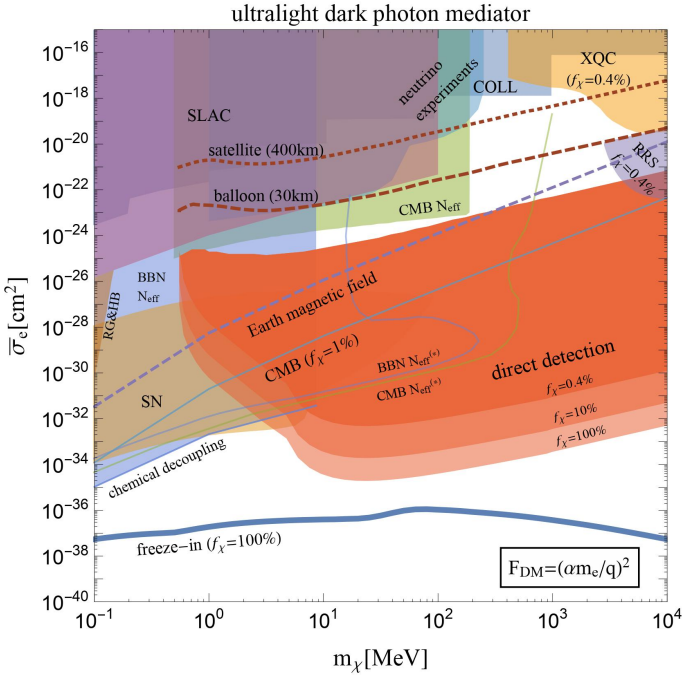

Figure 1.7: Constraints on dark matter interacting with a massive, ultralight dark photon are shown together with the discovery reach (thick red dashed lines) for a silicon dark matter detector with single-electron sensitivity on a balloon (satellite) assuming an exposure of 1 gram-hour (0.1 gram-month) and 10^6 (10^9) background events. The direct-detection constraints derived in this paper from SENSEI, CDMS-HVeV, XENON10, XENON100, and DarkSide-50 (combined into one red-shaded region, labelled "direct detection"). For a more detailed discussion about the different constraints please visit [33]. The region at high cross sections is unconstrained from CMB measurements if this dark matter particle only makes up a subdominant component ($f_\chi \lesssim 0.4\%$) of the total observed dark matter abundance. The figure and the caption are taken from [33].

The fact that the exclusion bounds in figure 1.7 do not fully exclude strongly interacting dark matter opens the opportunity to look for such interactions with experiments at the Earth's surface or preferably even above ground. These searches are currently led by silicon devices, like the SENSEI experiment [33]. In spring of 2020, the idea arose to use Xurich II, a small xenon TPC located at the University of Zurich, to study such interactions. The advantage of Xurich II with respect to other surface experiments, is that no xenon experiment at the surface was included in [33]. And, the detector had just received an upgrade and was calibrated with a very low energetic source [36]. The above reasoning lead to the question if new parameter space can be excluded with an above ground xenon experiment. Before moving on to the detailed description of Xurich II and its working principle a short introduction to the SENSEI experiment will be given.

1.5.1 SENSEI

SENSEI is a silicon-based experiment that looks for dark matter electron interactions with a Skipper-Charge-Coupled-Devices (Skipper-CCDs). The experiment consists of millions of pixels, in which electrons from the valence band can be promoted to the conduction band by a particle absorption or scattering. The 1.1 eV silicon band gap allows for direct detection of particles down to $\sim$ 500 keV through scattering and for the detection via absorption of dark matter with masses above the band gap. An excited electron in the conduction band subsequently relaxes to the bottom of the band, creating an additional electron-hole pair for each 3.8 eV of excitation energy above the band gap. The electron-hole pairs are later moved to one of the ultralow-noise readout stages that measure the charge content of each pixel with very high precision by repeated measurement. The Skipper-CCD is housed in a copper vessel and is operated at a low temperature to reduce the dark current that stems from thermal fluctuations. Even though the Skipper-CCD is very light and the technique is relatively young, SENSEI already yields the current best exclusion bounds for light fermionic dark matter that interacts via a ultralight dark photon [27], see the right panel in figure 1.6.

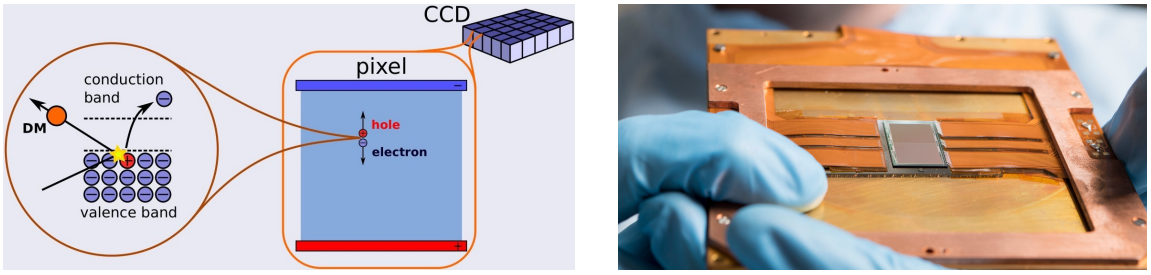

(a) Detection principle

(b) Prototype Skipper-CCD

Figure 1.8: Left: Detection principle of the Skipper-CCD technique. The big difference to a regular CCD is the possibility to measure the charge content of each pixel multiple times such that extraordinary resolution and single electron sensitivity can be reached. Right: Picture of the SENSEI prototype Skipper-CCD in the cooper housing with a size of roughly 10x20 mm and mass of 0.0947 grams [37].

Chapter 2

Xurich II: A Dual-Phase Xenon TPC

The following chapter introduces the detection principle of dual-phase xenon TPCs, explains the signal that light dark matter would create within them and shows an overview of the features of the Xurich II experiment.

2.1 Working Principle

The main goal of two-phase xenon TPC, is to detect an interaction between dark matter and ordinary matter, as a scattering process in liquid xenon. In the scattering process, the incoming particle transfers some kinetic energy to the xenon nucleus or an atomic electron surrounding the nucleus resulting in a mix of scintillation, ionization and heat. Of these, only the first two are detectable by dual-phase TPCs. The recoiling nucleus or electron, as it moves through the liquid xenon, creates a track of exited xenon atoms $Xe^{\star}$, xenon ions Xe^{+} and free electrons e^{-}. The exited xenon atoms $Xe^{\star}$ form so called *excimers* $Xe_2^{\star}$ which de-excite by disassociating and emitting scintillation light in the vacuum-ultraviolet (VUV) range (peak at 178nm). They create what is called the S1, prompt, light signal. This marks the first part of the detection process.

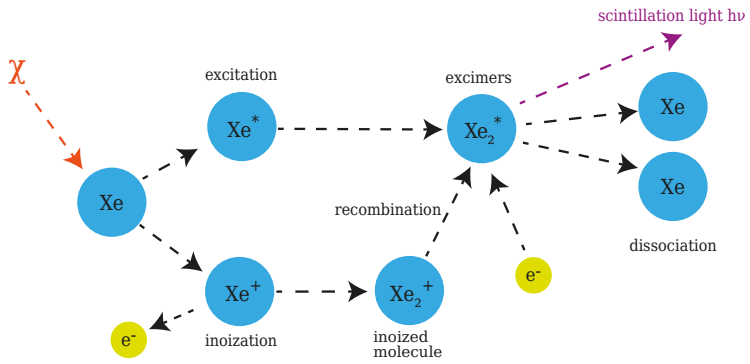

Figure 2.1: Interaction scheme of a dark matter (red) scattering or being absorbed by a xenon atom in the liquid phase (blue). Detectable signals are either the scintillation photons from the excimers $Xe_2^{\star}$ or the ionized electrons (yellow) that are drifted away from the interaction site by an electric field.

In the second part, the liberated electrons are drifted away from the interaction site by an electric field to be measured independently. The currently favored method of charge detection relies on electroluminescence to convert electrons into a proportional photon signal in the gas phase. To extract the electrons into the gas phase a strong electric field is applied over the liquid-gas interface and in the gas phase the second light signal, called S2, is created. The process is illustrated in figure 2.2 together with the resulting signals that are detected by photosensors located at the top and bottom of the chamber. The technique is sensitive to the extraction of single electrons due to the amplification in the gaseous xenon. A single electron can create up to $\mathcal{O}(1000)$ photons per centimeter of drift path depending on strength of the electric field [38]. The electroluminescence is a linear process because the energy is dissipated by the emission of photons which do not participate further in the electroluminescence [38]. The created photons are in the following measured by photosensors in which the photons are converted back into an electrical signal, namely electrons. The measured electrons in the photosensors are therefore called *photoelectrons* (PE) and the measured amount of PE is related to the initial recoil energy in the liquid xenon through the described mechanisms.

The S1 and S2 signal are not independent of each other and are linked through a process called *recombination*. Some electrons will recombine with xenon ions instead of moving away from the interaction site. The formed exited xenon atoms contribute to the S1 signal instead of to the S2 signal. This creates an anti-correlation between the S1 and S2 signal which is clearly visible in the S1-S2 parameter space. Since the fraction of liberated electrons contributing to either the S1 or S2 signal fluctuates even for interactions caused by monoenergetic sources, careful data analysis is required to calibrate the detector.

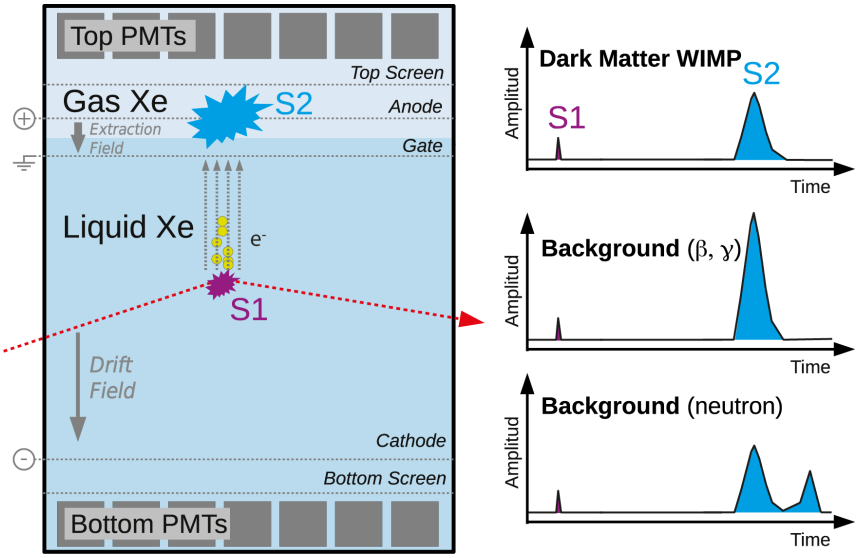

Figure 2.2: Working principle of a xenon dual-phase TPC. A particle interaction within the liquid xenon creates prompt scintillation light signal (S1) and a proportional photon signal from electroluminescence (S2) in the gas phase. The signals are detected by photosensors located at the top and the bottom. Illustration taken and adapted from [39].

A big advantage of dual-phase TPCs is the possibility to reconstruct the position of the interaction by using the light distribution of the second signal, the S2, and the time difference between the S1 and the S2 signal. This feature allows the experimentalist to study events that happened at a particular location, for example, the inner most part of the TPC, where fewer events happen due to the stopping power of the liquid xenon. This so-called *fiducialization* is an important technique that allows for mitigation of backgrounds events. Moreover, the type of the interaction can be studied by the S1/S2 ratio, see the different sizes of S1 and S2 for the different sources in figure 2.2. What is meant with the type of interaction is whether a xenon nucleus or an electron was hit by the incoming particle. In the case of the nucleus, one speaks of a nuclear recoil and sources of such a signal are for example neutrons or the most famous dark matter candidates, the WIMPs. If an atomic electron is the target one speaks of electronic recoil and the causing particles can be γ-rays or electrons from β-decays. The possibility to distinguish the two interactions is another important advantage of this search technique.

S2-only Signals

The size of the S1 signal normalized by the recoil energy, called light yield, decreases with decreasing electron recoil energy [40]. This means the detection of the S1 becomes increasingly difficult with decreasing recoil energy. The reason for this resides in the mechanism that creates the S1 scintillation light signal, see the upper path shown in figure 2.1. A xenon atom Xe is excited by an elastic scattering event to $Xe^{\star}$ that combines with another xenon atom from the surrounding to form an excimer $Xe_2^{\star}$, which later de-exites by dissociating into two Xe atoms and scintillation light. Therefore less scintillation light is produced if the initial scattering creates less excited xenon atoms $Xe^{\star}$. This means the S1 gets smaller with decreasing energy and at some point, it will fall below the detection threshold. The detection threshold is influenced by instrumental parameters for example the trigger threshold or the light collection efficiency.

The so-called *S2-only* events, where no S1 is detected, are the anticipated signals for a sub-GeV dark matter interacting with an atomic electron. A xenon TPC, which is set up to measure light and charge, becomes in this case an experiment that only measures charge. The smallest detectable signal in this case is single electron ionization. The single electron signals are of special interest because they mark the low energy limit of this detection technique and the limit is defined by the minimal energy required to ionize a xenon atom, which is the smallest binding energy 12.4 eV. With only the charge signal, important information is missing and a couple of powerful analytical techniques to remove background events or correct the signals do not work. It is for example not possible to reconstruct the depth of the event with the time difference between the S1 and the S2 signals. It is not possible either to apply corrections due to charge losses during the drifting of the electrons.

Why Xenon?

Xenon is the rarest non-radioactive element on Earth and can only be found in the atmosphere. It is a heavy element with a mean atomic mass off 122 $\mathrm{GeV/c^2}$ [1]. The resulting liquid density, which is roughly three times the one of water, enables the construction of a relatively small detector with a high mass. Due to the linear dependence of the stopping power on the absorber density, there is a strong self-shielding effect that creates a region of very low background in the innermost part of the detector. The mass of the xenon nucleus is kinematically ideal for the momentum transfer with a WIMP in the mass range above a few $\mathrm{GeV/c^2}$. Another advantage, concerning dark matter searches, is the large number of natural xenon isotopes. The variety of isotopes creates diverse nuclear properties which give sensitivity to various interaction models, be it spin-independent or spin-dependent. The different xenon isotopes additionally open the possibility of other interesting physic searches, for example, the rare double electron capture of ^{124}Xe [41] or the hypothesized neutrinoless double-beta decay in ^{136}Xe [42]. The excellent scintillation properties and the relatively high boiling point add what is necessary to make an experiment technically feasible. The scintillation light of xenon has a wavelength of 178 nm, which is directly detectable with VUV sensitive photomultiplier tubes (PMTs) or silicon photomultipliers (SiPMs).

2.2 The Xurich II Detector

The Xurich II detector is a small dual-phase xenon TPC at the University of Zurich that is used to test new developments like new photosensors or calibrations with new sources. It has shown stable working conditions in multiple calibration runs [43, 36]. The detector received an upgrade in 2018 and is now equipped with an array of 16 SiPM at the top and one 2-inch PMT at the bottom. Additionally, a gas system for calibration with ^{37}Ar was installed with the upgrade. The SiPM array allows for a position reconstruction in the horizontal plane (x,y) with a resolution of about 1.5 mm, assuming the z-axis to be aligned with the rotation axis of the cylindrical chamber. The cylindrical drift region has a size of 31 mm × 31 mm (diameter × height) and contains a mass of liquid xenon of roughly 68 g, see figure 2.3 for an overview of the detector and its components.

Seven copper field-shaping rings, enclosed by a polytetrafluoroethylene (PTFE) shell and connected by a resistor chain, ensure a uniform drift field between the negatively biased cathode at the bottom and the gate at ground potential. The drift fields strength can be varied by changing the cathode voltage. It was set to -3 kV for the relevant data set, which results in a relatively high drift field of 968 V/cm. The hexagonal gate and anode mesh are separated by 4 mm and the liquid level is kept in the middle, around 2 mm above the gate. The extraction field between the gate and the positively biased anode is kept constant at 10 kV/cm by applying +4 kV to the anode. The field strength in the liquid and the gas phase is slightly different due to the difference in the dielectric constant of the two phases. The detector is placed inside a vacuum-insulated stainless steel vessel that is coupled to a liquid nitrogen bath via a copper cold finger.

[1] $1\,\mathrm{GeV/c^2} = 1.782662 \cdot 10^{-27}$ kg

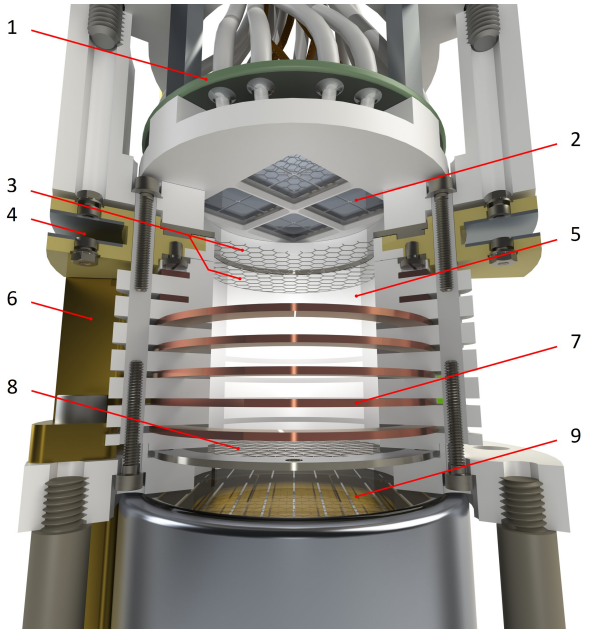

Figure 2.3: Rendering of the upgraded Xurich II TPC. The active liquid xenon is contained within a PTFE cylinder and surrounded by copper field-shaping rings. A 2-inch PMT (R9869MOD, Hamamatsu Photonics) is placed in the liquid, and an array of 16 SiPMs is placed in the gaseous phase at the top. For the sake of visualization, two field-shaping rings have been cut. Legend: 1 - PCB with x10 preamplifier, 2 - SiPM array (2×2 array of S13371, Hamamatsu Photonics), 3 - Anode and gate mesh, 4 - Level meters, 5 - PTFE reflector wall, 6 - Weir for liquid level control, 7 - Copper field-shaping rings, 8 - Cathode, 9 - PMT. The figure and the caption are taken from [36].

2.2.1 Calibration of the Xurich II detector with ^{37}Ar

Gaseous ^{37}Ar can be inserted into the gas recirculation system to perform an energy calibration at low energies. ^{37}Ar decays via electron capture to stable chlorine ^{37}Cl and a neutrino ν_e with a half-life time of 35.7 days [36]. The difference in the binding energy of the two atoms, the so-called Q-value, is converted into the neutrinos kinetic energy and accounts for $813.9 \pm 2\,\text{keV}$ [44]. The remaining electron vacancy is subsequently filled whereby X-rays and Auger electrons are ejected creating a measurable signal. See figure 2.4 for an illustration of the process and table 2.1 for the corresponding energies.

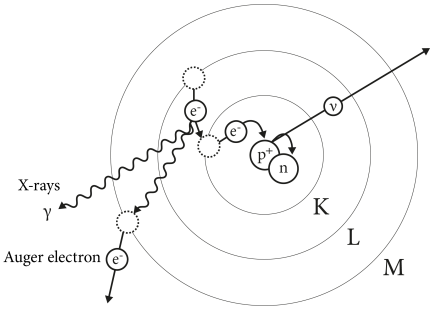

Figure 2.4: Illustration of the decay via electron capture.

Decay mode	Energy release [keV]	Branching ratio
K-capture	2.8224	90.2%
L-capture	0.2702	8.9%
M-capture	0.0175	0.9%

Table 2.1: Energy release and branching ratios of decay modes of ^{37}Ar [45].

The energy of an electronic recoil event is computed as the sum of created photons n_γ and electron n_e multiplied with W the average energy required to either create a photon or an electron [2]. The formula shown in equation 2.1 can be rewritten in terms of the signals S1 and S2 but two unknown detector-specific parameters, called g_1 and g_2, have to be introduced. The exact determination of these two factors is the goal of the energy calibration.

$$E = W(n_\gamma + n_e) = W\left(\frac{S1}{g_1} + \frac{S2}{g_2}\right) \tag{2.1}$$

The first step in the calibration is the identification and the determination of the mean S1 and S2 signals of the ^{37}Ar K-shell signals. The means are derived from a two dimensional Gaussian fit to the data in the S1 vs. S2 parameter space. In the left panel of figure 2.5 a 2D histogram of ^{37}Ar K-shell events from the latest calibration run is shown [36]. The red ellipses are the contour lines (1,2 and 3 σ) of the two dimensional Gaussian fit. By measuring the mean S1 and S2 of sources with different decay energies and/or by changing the strength of the drift field, the detector specific parameters g_1 and g_2 can subsequently be derived from the so called *Doke-plot*. The axes in this plot, the light and charge yield, are the mean S1 and S2 signals divided by the decay energy respectively. The linear anti-correlation of the light and charge yield allow the computation of g_1 and g_2 from the slop and the axis intersection. In the right panel of figure 2.5 the Doke-plot from the latest calibration run and the resulting values for g_1 and g_2 are shown. For more details including the discussion about the calibration with ^{83m}Kr please have a look at [36].

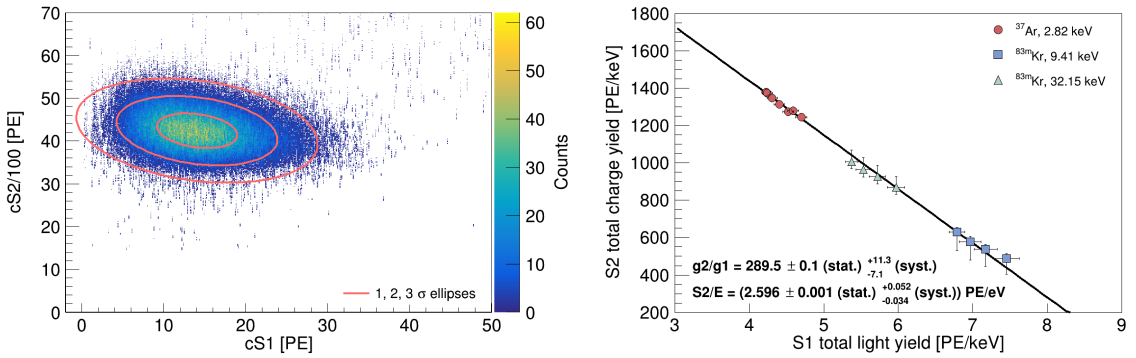

Figure 2.5: Left: 2D histogram of S1 vs. S2 of ^{37}Ar K-shell events shown together with the 1,2 and 3 σ contour lines (red ellipses) of a two dimensional Gaussian fit. Right: Doke-plot showing the anti-correlation of charge and light yield at different drift fields in the range 80 - 968 V/cm for ^{37}Ar and 194 - 968 V/cm for ^{83m}Kr, respectively. From axis intersection and the slope of the linear fit the detector-specific gains $g1$ and $g2$ can be computed. The figures are taken from [36] and [47].

[2] Historically W has been considered to be 13.7 ± 0.2 eV [46] but recently there has been a new measurement with the Xurich II detector and a slightly lower value of $11.5^{+0.2}_{-0.3}$ eV has been measured [47].

2.2.2 Measurements and Run Conditions

In the latest run in 2019, ^{37}Ar was used as an intrinsic calibration source and data was taken from mid-May until mid-November in 2019. On the 15th of May ^{37}Ar was injected into the gas recirculation system and a source activity of 2.7 kBq was estimated [36]. To measure the relatively long half-life of ^{37}Ar, data had to be taken for a relatively long time (>100 days). The data set of interest, called "background data" was taken more than 4 half-lives after the initial injection, which implies that the event rate due to the ^{37}Ar had been reduced to 1/16 of the initial.

Throughout the data taking, gain calibrations were performed and stable PMT and SiPM gains were observed. For the PMT at the bottom an average gain of $(3.76 \pm 0.06) \times 10^6$ was measured and for the SiPM array an average of $(3.12 \pm 0.01) \times 10^7$ including the preamplifier with a tenfold amplification. The liquid xenon was continuously purified by a hot metal getter and electron lifetime of around 130 μs was reached. Overall one can view Xurich II as a small xenon TPC with high drift and extraction fields and acceptable xenon purity.

Chapter 3

Dark Matter Electron Scattering

The missing trace of WIMPs and the possibility of looking for lighter dark matter with existing experiments has caused alternative explanations to gain in popularity. One group of models, the so-called *hidden sector models*, assume an unknown physics in the dark sector that couples to the standard model through a mediator, often called *portal*, containing one or more states that mediate between the Standard Model and the dark sector. The following section is mostly based on reference [33] which in turn is based on references [34, 30, 48, 49].

3.1 Rate Calculation

A simple dark sector model has a $U(1)_D$ symmetry and couples to the Standard Model through a dark photon A', which is also an undiscovered entity. The Lagrangian of this simple symmetry, containing a fermionic dark matter candidate χ with mass m_χ, can be written as:

$$\mathscr{L}_D = \bar{\chi}(i\gamma^\mu D_\mu - m_\chi)\chi + \frac{1}{4}F'_{\mu\nu}F'^{\mu\nu} + m^2_{A'}A'_\mu A'^\mu + \frac{\varepsilon}{2}F_{\mu\nu}F'^{\mu\nu} \tag{3.1}$$

with the covariant derivative

$$D_\mu = \partial_\mu - ig_D A'_\mu \tag{3.2}$$

and the field strength tensors

$$F_{\mu\nu} = \partial_\mu A_\nu - \partial_\nu A_\mu, \qquad F'_{\mu\nu} = \partial_\mu A'_\nu - \partial_\nu A'_\mu \tag{3.3}$$

with g_D the gauge coupling of the $U(1)_D$ gauge group and ε the kinetic mixing parameter. In the term $\varepsilon F_{\mu\nu}F'^{\mu\nu}$ the coupling between the Standard Model and the dark sector is described. In this term, the dark photon A' and the standard model photon A mix and generate the interaction. The kinetic mixing creates an interaction between the dark sector and all charged fermions in the Standard Model. The relevant interactions for an experiment, the interactions to protons p and to electrons e, are parametrized as follows.

$$\mathscr{L}_{int} = e\varepsilon A'_\mu \left(\bar{p}\gamma^\mu p - \bar{e}\gamma^\mu e\right) \tag{3.4}$$

The dark matter-electron differential scattering cross section can be expressed as:

$$\frac{\mathrm{d}\sigma_e}{\mathrm{d}q^2} = \frac{4\pi\alpha\alpha_D\epsilon^2}{(q^2+m_{A'}^2)^2}\frac{1}{v^2} \tag{3.5}$$

where $\alpha \equiv e^2/(4\pi)$ is the fine structure constants of the Standard Model and $\alpha_D \equiv g_D^2/(4\pi)$ the fine structure constant of the dark sector. q is the momentum transfer of the dark matter to the electron and v is the relative speed between the nucleus and dark matter particle. The differential scattering cross-section between dark matter and a nucleus ${}^A_Z N$ in this model is given by

$$\frac{\mathrm{d}\sigma_N}{\mathrm{d}q^2} = \frac{4\pi\alpha\alpha_D\epsilon^2}{(q^2+m_{A'}^2)^2}\frac{1}{v^2}F_N(q)^2Z^2 \tag{3.6}$$

$F_N(q)$ is the nuclear form factor, which accounts for the loss of coherence for large momentum transfers. Furthermore a reference cross section for dark matter-electron and for dark matter-proton scattering are defined.

$$\bar{\sigma}_e \equiv \frac{16\pi\alpha\alpha_D\varepsilon^2\mu_{\chi e}^2}{(q_{\mathrm{ref}}^2+m_{A'}^2)^2} \tag{3.7}$$

$$\bar{\sigma}_p \equiv \frac{16\pi\alpha\alpha_D\varepsilon^2\mu_{\chi p}^2}{(q_{\mathrm{ref}}^2+m_{A'}^2)^2} \tag{3.8}$$

q_{ref} is chosen to be αm_e, the typical momentum transfer in dark matter-electron scattering for noble-liquid and semiconductor targets. Notice that the definition 3.7 and 3.8 merge the effect of 4 entities $(\alpha_D, \epsilon, m_{A'}, m_\chi)$ without specifying them individually. The ratio of the two reference cross-sections does not depend on the choice of the reference momentum transfer and introduced a hierarchy between the interaction with electrons and protons.

$$\frac{\bar{\sigma}_p}{\bar{\sigma}_e} = \left(\frac{\mu_{\chi p}}{\mu_{\chi e}}\right)^2 \tag{3.9}$$

μ_{ij} denotes the reduced mass of particle i and j, and for light dark matter masses ($\mathcal{O}$(MeV)) the cross section for the interactions with proton dominates over the interaction with electrons. Equation 3.9 indicates that dark matter-nucleus scatterings in the Earth's crust and atmosphere can become non-negligible for dark matter-electron scattering experiments [50, 49]. It is furthermore useful to write the differential cross section in terms of the reference cross section $\bar{\sigma}_e$,

$$\frac{\mathrm{d}\sigma_e}{\mathrm{d}q^2} = \frac{\bar{\sigma}_e}{4\mu_{\chi e}^2 v^2}F_{\mathrm{DM}}(q)^2\,, \tag{3.10}$$

with the dark matter form factor

$$F_{\mathrm{DM}}(q) = \frac{q_{\mathrm{ref}}^2+m_{A'}^2}{q^2+m_{A'}^2}\,, \tag{3.11}$$

which parametrizes the q dependence. Two cases naturally emerge from this formula.

$$F_{\rm DM}(q) = \begin{cases} 1 & \text{for } m_{A'}^2 \gg q_{\rm ref} \text{ a heavy mediator, contact interaction} \\ \frac{(q_{\rm ref})^2}{q^2} & \text{for } m_{A'}^2 \ll q_{\rm ref} \text{ a ultralight mediator, long range interaction} \end{cases} \tag{3.12}$$

For atomic targets such as liquid xenon or argon, the ionization rate requires the sum over the differential scattering cross sections of the electron in the shell (n,l), to an excited or ionized final state with energy E_{er}, according to the following equation.

$$\frac{{\rm d}R}{{\rm d}E_{er}} = N_T \frac{\rho_\chi}{m_\chi} \sum_{nl} \frac{{\rm d}\langle\sigma_{ion}^{nl}\rangle}{{\rm d}\ln E_{er}} \tag{3.13}$$

N_T denotes the number target atoms, ρ_χ the dark matter density and $\langle\sigma_{ion}^{nl}\rangle$ the velocity averaged cross section. The differential cross section for the electron with quantum numbers (n,l) requires the integral over the transferred momentum q with $|f_{ion}^{nl}(k',q)|^2$ the squared ionization form factor, which describes the likelihood that a given momentum transfer results in a particular electron recoil energy. $k' = \sqrt{2m_e E_{er}}$ denotes the momentum of the escaping electron after receiving the momentum transfer q.

$$\frac{{\rm d}\langle\sigma_{ion}^{nl}\rangle}{{\rm d}\ln E_{er}} = \frac{\overline{\sigma}_e}{8\mu_{\chi e}^2} \int q\, {\rm d}q\, |f_{ion}^{nl}(k',q)|^2\, |F_{DM}(q)|^2\, \eta(v_{min}) \tag{3.14}$$

$\eta(v_{min})$ denotes the inverse mean speed, which is the integral over the normalized velocity distribution $f(v)$.

$$\eta(v_{min}) = \int_{v_{\rm min}}^{v_{\rm max}} dv \frac{f(v)}{v} \tag{3.15}$$

The maximum velocity $v_{\rm max}$ is given by $v_{\rm max} = v_{\rm earth} + v_{\rm esc}$ which is the escape velocity of the dark matter halo transformed into Earth's reference frame [1]. The minimum speed v_{min} required to change a bound electron's energy by ΔE_{er} by a momentum transfer of q is

$$v_{\rm min}(q, E_{er}) = \frac{\Delta E_{er}}{q} + \frac{q}{2m_\chi}\,. \tag{3.16}$$

For the electron in the atomic shell (n,l), the transferred energy is $\Delta E_{er} = |E_{\rm b}^{nl}| + E_{er}$, where $E_{\rm b}^{nl}$ is the binding energy of the corresponding state.

The integral in equation 3.14 and the sum in 3.13 are the key elements in the rate calculation for the hypothesized interaction. The astrophysical understanding about the dark matter velocity distribution enters via the inverse mean speed $\eta(v_{min})$, the ionization form

[1] Explicitly the velocity is $v_{\rm max} = 240$ km/s $+544$ km/s [33]

factors describe the scattering dynamics on an atomic level and $\overline{\sigma}_e$, m_χ, $F_{DM}(q)$ incorporate the new physics model.

Alongside the possibility of computing some hypothetical interaction, a dark matter model also needs to be viable from a cosmological point of view. A mechanism that explains the creation of dark matter and the formation of the correct relic abundance is required. Next to the well-known freeze-out mechanism, where the constituents of the early universe start from thermal equilibrium, the freeze-in mechanism or initial asymmetries are alternative narratives with which hidden sector models can explain the correct relic abundance. The freeze-in mechanism, for example, assumes a situation where the dark sector, due to a very small coupling, never was in equilibrium with the Standard Model. Nevertheless, dark matter particles could still be produced from the thermal bath of the Standard Model [51, 52].

3.2 Dynamics in the Liquid Xenon

In xenon TPCs, the scintillation and ionization are the mechanisms that allow for the energy reconstruction of an event. From a recoiling electron, with energy E_{er}, a number of primary scintillation photons n_γ and a number of ionized electrons n_e are created and connected by

$$E_{\text{er}} = W(n_\gamma + n_e) \tag{3.17}$$

In the case of light dark matter ionizing an electron, only the number of electrons and the electroluminescence are important because the scintillation photons are assumed to be unobservable due to reduced light yield at low energies. This means that the rate of events as a function of energy E_{er} must be transformed into a rate depending on the number of electrons n_e. In a naive attempt one could try to convert the recoil energy into a number of electrons by the above relation, however this would not take into account the dynamics of the ionization process.

An electron that moves through the liquid xenon with a kinetic energy E_{er} can create additional free electrons on its trajectory to the liquid xenon surface by liberating other electrons through scattering (primary quanta) or if the initial interaction kicked out an inner shell electron, a relaxation-photon can liberate additional electrons (secondary quanta) in the surrounding liquid xenon. The number of primary quanta $n^{(1)}$ that result from the ionization track are computed as $n^{(1)}$=Floor(E_{er}/W). The number secondary quanta $n^{(2)}$ depends on the shell on which the initial electron was located at and account to $n^{(2)}$=($n_{5s}, n_{4d}, n_{4p}, n_{4s}$)=(0, 4, 6-10, 3-15). More details about the secondary quanta are given in table 3.1.

Shell	$5p^6$	$5s^2$	$4d^{10}$	$4p^6$	$4s^2$
Binding Energy [eV]	12.4	25.7	75.6	163.5	213.8
Photon Energy [eV]	–	13.3	63.2	87.9	201.4
Additional Quanta	0	0	4	6-10	3-15

Table 3.1: Xenon shells and energies. The "Photon energy" refers to the energy of de-excitation photons for outer-shell electrons de-exciting to lower shells. The range for the $4p$ and $4s$ shells takes into consideration that there is more than one outer-shell electron available that can de-excite down to the vacancy. For example, if the $4d$ shell de-excites to $4p$, 6 additional quanta are created, while if the $5s$ shell de-excites to $4p$, it would create 10 additional quanta. To be conservative, the lower number of quanta is considered. The table is taken from the appendix in [31].

A cloud of n_e electrons that moves upwards to the liquid-gas interface, is formed by the initial ionized electron and the electron fraction of the primary and secondary quanta. The probability for a quanta, either a photon or an electron, to be an electron can be described by a binomial distribution if the probability for a quanta to be an electron is known. Since the initial electron is already present, the conversion from the additional quanta needs to yield $n_e - 1$ electrons out of $n_q = n^{(1)} + n^{(2)}$ trials to end up with n_e electrons. This is described by the the following Binomial distribution.

$$B(n_e - 1|\, p = f_{\text{es}},\, n = n_q(E_{\text{er}})) \tag{3.18}$$

where f_{es} is the probability for a quanta to be observed as an electron, meaning the probability to create an electron and for it to survive until the measurement. This probability can be expressed as

$$f_{\text{es}} = (1 - f_R)\frac{N_i}{N_{\text{ex}} + N_i} \tag{3.19}$$

with N_i the number of ions and N_{ex} the number of excitons that are created by an interaction. f_{es} was measured to be $f_{es} \approx 0.83$ [53] and this value will be used in the following. So far the initial electron was believed to survive. However, there exists the probability that the initial electron recombines with an ion after moving through the liquid. f_R expresses this recombination probability and consequently $(1 - f_R)$ the survival probability. With that, the final equation for the probability to have n_e electrons in the liquid xenon from an scattering of an atomic electron in shell (n,l) with a recoil energy E_{er}, including both the survival and the recombination of the initial electron reads:

$$p_{n,l}(E_{\text{er}}) = (1 - f_R)\, B(n_e - 1|f_{\text{es}}, n_q(E_{\text{er}})) + f_R\, B(n_e|f_{\text{es}}, n_q(E_{\text{er}})) \in \mathbb{R}^{n_e} \tag{3.20}$$

Notice that the recombination probability for electrons from primary and secondary quanta is already considered in f_{es}. The function $p_{n,l}(E_{\text{er}}) \in [0, 1]^{n_e}$ relates the recoil energy E_{er} with the probability to measure an event with n_e number of electrons. To finalize the transformation from $\mathrm{d}R/\,\mathrm{d}E_{\text{er}}$ to $\mathrm{d}R/\,\mathrm{d}n_e$, the rate needs to be integrated over the recoil energy and then the contribution from all shells must be summed up:

$$\frac{\mathrm{d}R}{\mathrm{d}n_e} = \sum_{n,l} \int p_{n,l}(E_{\mathrm{er}}) \frac{\mathrm{d}R}{\mathrm{d}E_{\mathrm{er}}} \, \mathrm{d}E_{\mathrm{er}} \tag{3.21}$$

Given this conversion from E_{er} into n_e, the differential rate as a function of the number of electrons n_e can be computed. In figure 3.1, the individual contributions from each shell and the sum are shown before (left panel) and after the transformation (right panel). The figure was created with the publicly available code called *wimprates* [54, 29] that is based on [31]. The wimprates code was modified to accommodate the properties of the strongly interacting dark matter and used throughout the project to calculate the interaction rates. Notice how the contribution from the $4d$ shell that includes secondary quanta becomes dominating compared to the $5p$ shell which does not include any secondary quanta. The conversion was conducted assuming the recombination probability f_R to be effectively zero for low energies and in turn, the survival probability $(1 - f_R)$ is assumed to be 100%.

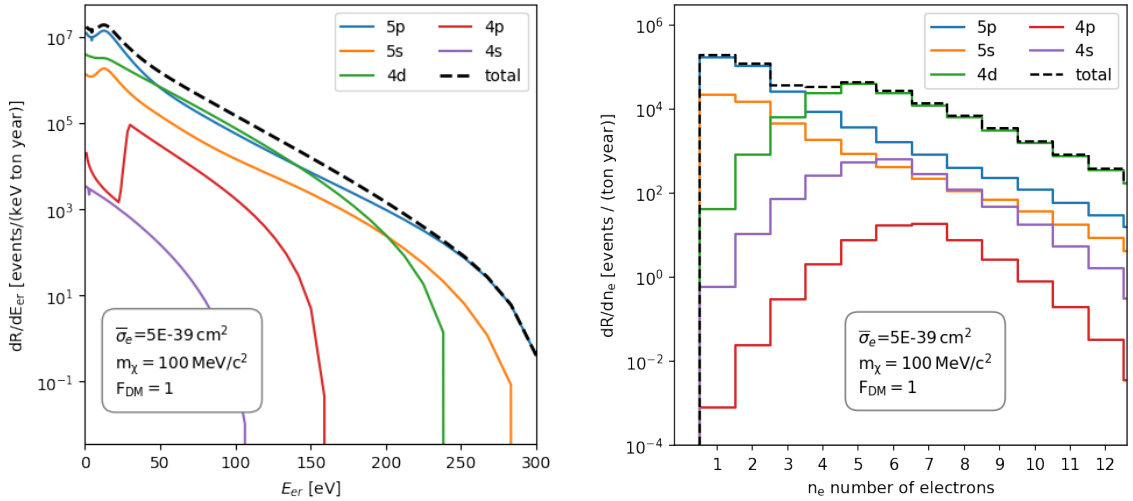

Figure 3.1: Event rate of a light dark matter-model interacting via a heavy dark photon assuming a dark matter velocity distribution according to the Standard Halo Model. In the left panel, the rate is shown as a function of the recoil energy E_{er} and in the right as a function on the number of electrons n_e. The rate as a function of E_{er} is not accessible in an experiment and needs to be converted to n_e as described in the text.

3.3 Attenuation

A crucial part of this analysis is the incorporation of dark matter scattering in the material above the experiment. In standard WIMP searches, this is not included because the WIMPs are assumed to have scattering cross sections at the weak scale and the interaction probability is small. This means that a change off the dark matter-flux at the interaction site is negligible. Large cross sections in contrast cause a different behavior and dark matter-electron, as well as dark matter-proton interactions, become very likely and a change in the flux of dark matter is expected. At first sight, this looks like a nuance but as will be shown, it causes a change in the interpretation of dark matter search results.

The scattering in the shielding materials can cause the dark matter to arrive at the detector with a reduced velocity such that recoil energies fall below the detection threshold or it can cause that dark matter does not reach the detector at all and is scattered away. Consequently, such candidates can not be probed for. The remaining part of the section will summarize the most important points of [49, 48, 33], a Monte Carlo (MC) study that was developed over a few years and that made it possible to quantify the effect of strongly interacting dark matter scattering in the overburden. Alongside the paper [33], the MC-simulation code (DaMaSCUS-CRUST [55]) was published and allows for the computation of the dark matter-flux for any given detector setup.

The basic idea of the MC simulation was to incorporate the detailed scattering dynamics of the different dark matter-models and then test the simplifying assumptions of analytic approaches. Analytic approaches, similar to the Bethe-Bloch formula, rely on the assumption of a continuous energy loss $\frac{\mathrm{d}E}{\mathrm{d}x}$ along a straight path from the crust of the Earth to the detector if the detector is placed underground. The extended path due to scattering, the unknown scattering dynamics for some of the dark matter-form factors and the importance of rare events can cause a significant difference to the analytic calculation.

The MC simulation's goal is the precise estimation of the dark matter speed distribution $f(v)$ at the detector's location. The starting point of that distribution is the *Standard Halo Model*, which assumes the dark matter velocity distribution is a Maxwell-Boltzmann distribution in the galactic rest frame. This represents an infinite isothermal sphere which is selfgravitating, does not rotate and creates a density profile $\rho \sim r^{-2}$, which yields the correct flat rotation curve at large radii. This distribution describes the fraction of the particles within an infinitesimal element of three-dimensional velocity space, d^3v, centered on a velocity vector of magnitude v, as $f(v)\ \mathrm{d}^3v$:

$$f(v)\ \mathrm{d}^3v = \frac{1}{v_0^3\pi^{3/2}}\exp(-v^2/v_0^2)\ \mathrm{d}^3v \tag{3.22}$$

where $v_0 \approx 220\,\mathrm{km/s}$ is the circular speed of the Sun around the Galactic center, more precisely the rotational speed of the local standard of rest (LSR). Without considering the motion of the Earth one would change to spherical coordinates and integrate over the angles to find:

$$f(v)\ \mathrm{d}v = \frac{4}{v_0^3\sqrt{\pi}}v^2\exp(-v^2/v_0^2)\ \mathrm{d}v \tag{3.23}$$

To transform this distribution into Earth's rest frame a Galilean transformation is used

$$\mathbf{v} = \mathbf{w} + \mathbf{v_e} \qquad v = w^2 + v_\mathrm{e}^2 + 2wv_e\cos\theta \tag{3.24}$$

with $\mathbf{w}$ the speed of dark matter with respect to Earth's rest frame, $\mathbf{v_e}$ Earth's velocity in the galactic rest frame and θ the angle between the dark matter's velocity the Earth's frame and the direction of the Earth's motion. At this point, Earth's orbit around the Sun could additionally be considered and that would create a signal modulation that changes

throughout the year but here the time of the experiment is not specified and v_e is set to $v_e \approx 240$ km/s. The Galilean transformation requires an integration over the angle θ which unfortunately is not well documented in the literature but the following result was found in [56].

$$f(w)\,\mathrm{d}w = \Big(\frac{w}{v_e v_0 \sqrt{\pi}}\Big)\Big[\exp\big(-\frac{(w-v_e)^2}{v_0^2}\big) - \exp\big(-\frac{(w+v_e)^2}{v_0^2}\big)\Big]\,\mathrm{d}w \tag{3.25}$$

As dark matter particles with a velocity faster than the escape velocity $v_{\mathrm{esc}} = 544$ km/s [57] are fast enough to escape the gravitational pull of the Milky Way, the distribution needs to be truncated. One common mathematical solution for such a problem is to multiply the distribution with a Heaviside-function but this results in an unphysical unwanted edge. An ad-hoc solution that can be used to smooth the distribution in 3.25 is to add an additional term [58] as shown in the next equation. Adding a new term requires a reevaluation of the normalization constant even though the change is only noticeable at the high velocity tail of the distribution. See the right panel in figure 3.2 for the comparison between the two distributions and the high velocity tail.

$$f(w)\,\mathrm{d}w \approx \Big(\frac{w}{v_e v_0 \sqrt{\pi}}\Big)\Big[\exp\big(-\frac{(w-v_e)^2}{v_0^2}\big) - \exp\big(-\frac{(w+v_e)^2}{v_0^2}\big) - \underbrace{\exp\big(-\frac{v_{\mathrm{esc}}^2}{v_0^2}\big)}_{\text{smoothing}}\Big]\,\mathrm{d}w \tag{3.26}$$

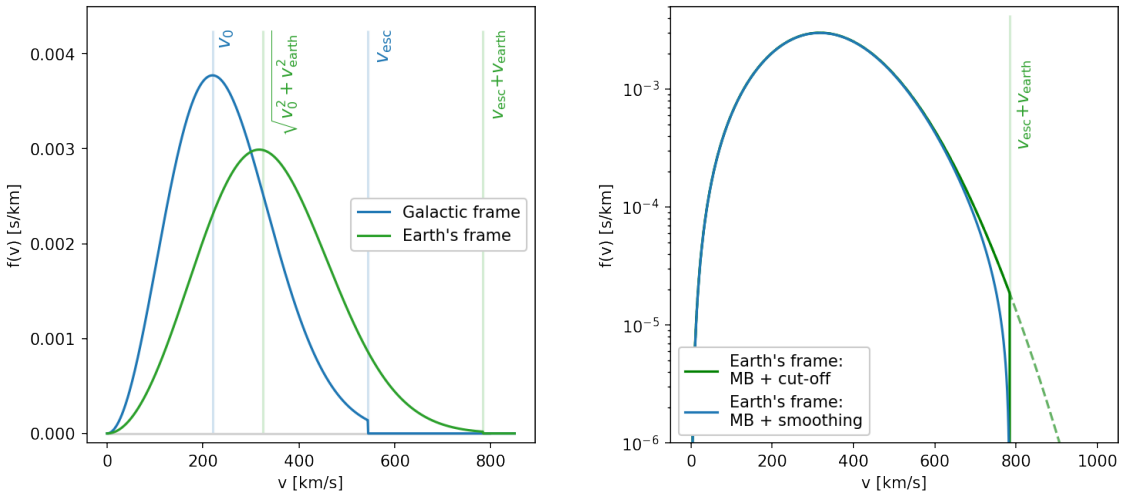

Figure 3.2: Left: Velocity distribution of the *Standard Halo Model* (blue) in the Galactic rest frame transformed into the rest frame of the Earth (green). Right: The Maxwell-Boltzmann velocity distribution in Earth's rest frame including a sharp cut-off (green) and the distribution from 3.26 which includes the smoothing term (blue). The distributions are drawn on a semi-logarithmic scale to emphasize the differences in the high velocity tails.

If the scattering in the overburden is negligible, $f(v)$ is the speed distribution from the smoothed Standard Halo model in equation 3.26 [2] and is used to sample the initial conditions of the incoming dark matter. Subsequently, the expected rate in the experiment can

[2] In the MC simulation [55] a different parametrization is used but essentially it is the distribution from 3.26 with the correct normalization constant.

be calculated with equation 3.13 and 3.14. The dark matter path from the Earth's surface to a given underground depth is basically a random-walk where each particle starts with an initial velocity in the z-direction and gets deflected and decelerated by scattering in the material. It is important to note that in the simulation the scattering is performed until either the particle gets reflected into space, gets decelerated below the minimum speed, or reaches the detector. If it reaches the detector the velocity is saved and will account to the new underground speed distribution. The minimum speed depends on the experiment's energy threshold E_{thr} [3], resolution σ_E as well as on the mass of the target atoms m_T.

$$v_{\text{min}} = \sqrt{\frac{m_T(E_{\text{thr}} - 3\sigma_E)}{2\mu_{\chi T}^2}} \tag{3.27}$$

As the dark matter models discussed in this chapter introduce interactions with all charged particles and particularly with electrons and protons, a few different scatterings interactions are possible. There can be elastic and inelastic scattering on atomic electrons, which can cause excitation and ionization of electrons, as well as elastic scattering on protons in the nucleus. In figure 3.3 the exclusion bounds from a simulation of the different scattering interactions are compared for an example experiment placed 2km below the surface with silicon as a target. As visible, the stopping due to scattering off nuclei dominates over the stopping due to scattering on atomic electrons and between the MC-simulation and the analytic approach a noticeable difference appears especially for light dark matter candidates.

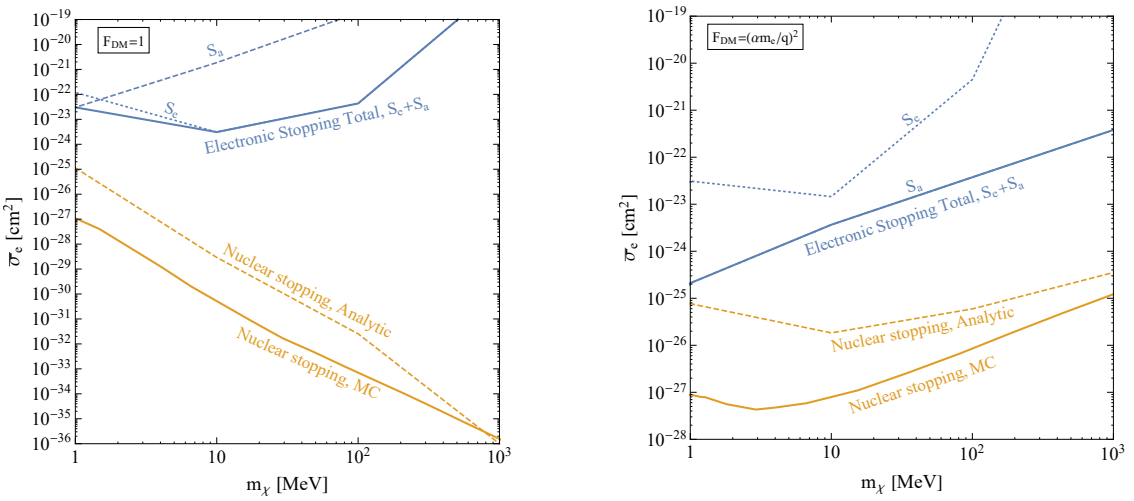

Figure 3.3: Comparison of dark matter stopping through interactions with electrons (blue curves) versus interactions with nuclei (yellow curves) for heavy mediator case (left panel) and the light mediator case (right panel). Evaluated for a generic silicon experiment with a threshold of one electron-hole pair, an exposure of 100 gram-year, and placed 2 km underground. The critical cross sections based on the ionization stopping power (dotted line, labeled S_e) and atomic scattering (dashed line, labeled S_a) are shown separately, while the critical cross section based on the total stopping power is shown by the thick line. The figure and the caption are taken from [33].

[3] For the Xurich II detector which has single electron sensitivity the energy threshold was set to $12.4eV$, the smallest binding energy of the $5p$ shell.

In figure 3.4, the results of the MC simulation for an example silicon experiment placed 1 km below the surface are shown [33]. In the left panel, the change in the velocity distribution $f(v)$ with changing interaction cross section $\bar{\sigma}_e$ is shown and a very strong attenuation becomes evident. In the right panel, the number of expected events as a function of the interaction cross section is displayed. The curve shows the same effect as in the left panel but the sudden loss of sensitivity is more apparent.

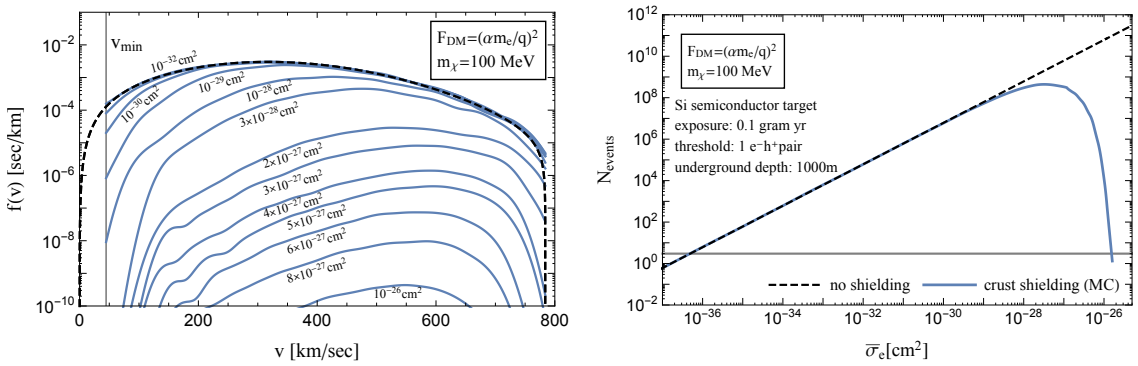

Figure 3.4: The left panel shows the distortion of the dark matter speed distribution due to underground scatterings on nuclei in 1 km of rock overburden obtained with MC simulations. The labels indicate the respective values of $\overline{\sigma}_e$. The right panel shows the resulting attenuation of the number of expected events in a generic semiconductor experiment. The figure and the caption are taken from [33].

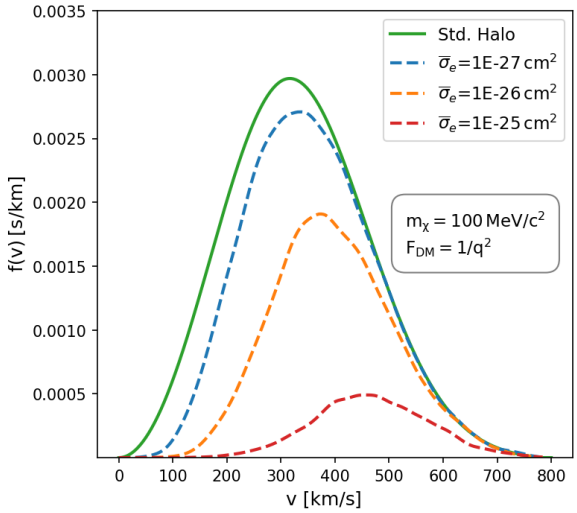

Figure 3.5: Velocity distribution of the Standard Halo Model (green line) and the velocity distributions (blue, orange and red dashed lines) after dark matter scattered in the overburden of Xurich II. Dark matter is assumed have to following properties: $m_\chi = 100\,\mathrm{MeV/c^2}$, $F_\mathrm{DM} = 1/q^2$ and $\bar{\sigma}_e = 10^{-27}\,\mathrm{cm}^2$ (blue), $10^{-26}\,\mathrm{cm}^2$ (orange) and $10^{-25}\,\mathrm{cm}^2$ (red).

In the simulation code, the Earth's crust, the atmosphere, and the shielding layers are represented as planar layers because close to the critical cross section particles reach the

detector virtually exclusively from directly above. The effect of the overburden for Xurich II was simulated using DaMaSCUS-CRUST with the following layers: the atmosphere, 2.5 m of concrete due to the roof and floors of the building, and 4.4 cm of steel from the vessel and flanges. In figure 3.5 the effect of dark matter scattering in these layers is shown.

3.4 Modulation

A possible signature with which dark matter could actually be *discovered* would be the annual modulation of the measured interaction rate due to the motion of the Earth relative to the dark matter halo. The relative velocity between the Earth and the dark matter particles in the halo of the Milky Way depends on the time of year and varies by about ± 15 km/s from summer to winter. Hence, the measured number of events is expected to show an increase and decrease in a sinusoidal fashion over the time of a year. The fractional modulation amplitude f_{mod} is defined as:

$$f_{\text{mod}} = \frac{R_{\text{max}} - R_{\text{min}}}{2R_{avg}} \tag{3.28}$$

where R_{max} (R_{min}) is the maximal (minimal) rate throughout the year and R_{avg} is the average rate. In figure 3.6 the expected spectrum of f_{mod} as a function number of electrons n_e is shown and a modulation of up to 30% in case of light dark matter is predicted.

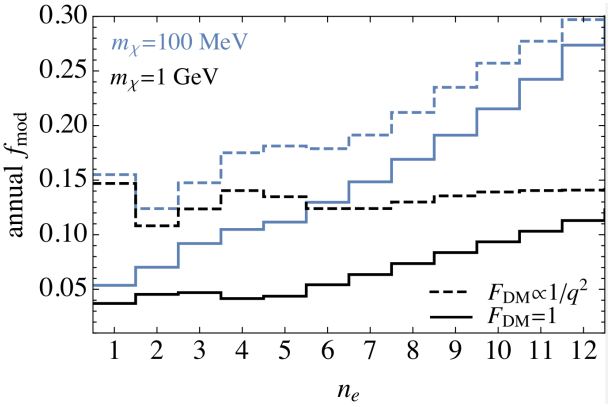

Figure 3.6: Annual fractional modulation for $F_{\text{DM}} = 1$ (solid) and $F_{\text{DM}} = 1/q^2$ (dashed) for $m_\chi = 100$ MeV (blue) & 1 GeV (black). The figure and the caption are taken from [31].

Together with to the annual modulation, there is also a expected daily modulation but since the rotation velocity of the Earth only changes the relative velocity by ± 0.23 km/s, the impact is anticipated to be about an order of magnitude smaller than the annual modulation [31]. In the case of strongly interacting dark matter, a much stronger daily modulation is expected than the one from the change of relative velocity by the Earth's rotation. Dark matter scattering in the Earth would create a strong modulation and especially the flux of fast dark matter particles can significantly be reduced, as all particles from the high-speed tail approach the experiment from the same direction. This so-called

Earth's shadow and the relative speed between experiment and dark matter, create a potential tool to discriminate between the dark matter signal and backgrounds but require large data sets, ideally multiple years. For strongly interacting dark matter much smaller data sets could be useful due to the daily modulation and such an analysis is in principle possible with the data from Xurich II. However, this topic is beyond the scope of this thesis. As discussed in [33] there exists even the idea to use balloon or satellite borne experiments to pick up the modulation with different frequencies depending on the period of the orbit.

Summary

Overall the chapter introduced the dark matter candidate, clarified the computation of the expected scattering rate and the conversion into a detectable signal, and introduced the effect of scattering in the overburden. Additionally, the signal modulation coming from Earth's movement was briefly discussed. The wimprates code will in the following be used to compute the expected event rate for a given set of dark matter-model parameters: F_{DM}, $\overline{\sigma}_e$,m_χ and the underground velocity distribution $f(v)$ that is computed using DaMaSCUS-CRUST.

Chapter 4

Backgrounds

In this chapter, the relevant backgrounds for single to a few electron events are reviewed and put into the perspective of the Xurich II experiment. The interpretation that some of the small S2 signals are caused by dark matter, as described by the theory in the previous chapter, is possible because there are no concise, quantitative descriptions of the known mechanisms that can cause these signals in liquid xenon TPCs. The known mechanisms are the photoelectric effect on the metal grids, field emission from the metal grids and photoionization of impurities [59].

4.1 Photoelectric Effect and Photoionization

The most prominent single electron population is known to follow immediately after an S2. The delayed signals are composed of individual electrons with a rate that decreases over time and after the maximum drift time Δt_{max}, a sharp drop-off is usually observed, see as an example the drop-off after $325\,\mu s$ in figure 4.1. The strong time correlation is evident and the emission from the photoelectric effect on the gate and the cathode are identified from the timing. These emissions are possible because the xenon scintillation light energy ($\sim 7\,\mathrm{eV}$) is higher than the work function of stainless steel ($\sim 4.3\,\mathrm{eV}$ [60]). Notice that the copper field shaping rings in the Xurich II detector are shielded from the scintillation light by a PTFE reflector and without this cover, many more single electrons would be observed.

The signals, between the grid emissions in figure 4.1, are attributed to the photoionization of impurities due to the lower rate after the maximal drift time [61, 59]. Drifting upwards in the liquid xenon, electrons can be attached to electronegative impurities [1], described by the following reaction.

$$e^- + S \longrightarrow S^{-\star} \tag{4.1}$$

Electron attachment to a neutral molecular system S is the result of a delicate balance between attractive electrostatic, polarization and electron electron repulsion interactions. If the quantum well resulting from the sum of those attractive and repulsive terms is deep enough to support a bound state, the excess electrons can be trapped in a very diffuse orbital. This orbital is not a localized valence orbital of the parent but is located outside

[1] The electronegativity describes the tendency of an atom to attract electrons to itself and not the fact that they are negatively charged.

the molecular cloud of the accepting molecule. This special type of bond is relatively week and small energies < 1eV are enough to liberate the electron [62]. The excited molecular system $S^{-\star}$ is not necessarily stable and can auto-detach the electron or break into fragments but if the excess energy can be passed to a collision partner in the surrounding, the system can stabilize with respect to electron auto-detachment and form a stable anion S^-. Even with the explained mechanism, there are molecules such as N_2 and H_2O that do not form stable anions [63].

The term photoionization describes the freeing of this specially bound electron by $S^- + h\nu \rightarrow S + e^-$ and commonly used in the physics community. Unfortunately it is not precise and should be called *photodetachment of anions* because the process is quite different from a normal ionization process $S + h\nu \rightarrow S^+ + e^-$ which requires significantly more energy due to the necessary charge separation. This can be seen in neutral impurity molecules such as O_2, N_2, and H_2O which usually have ionization energies above 10 eV and can therefore not be ionized by the xenon scintillation light [64].

Additional experimental evidence for the involvement of impurities comes from the XENON100 experiment, where a positive correlation between the single electron rate and the O_2 equivalent impurity level was reported [65]. Consistent with the electron detachment hypothesis is also the fact that the single electron emission occurs not only after an S2 but also after an S1 [65, 59].

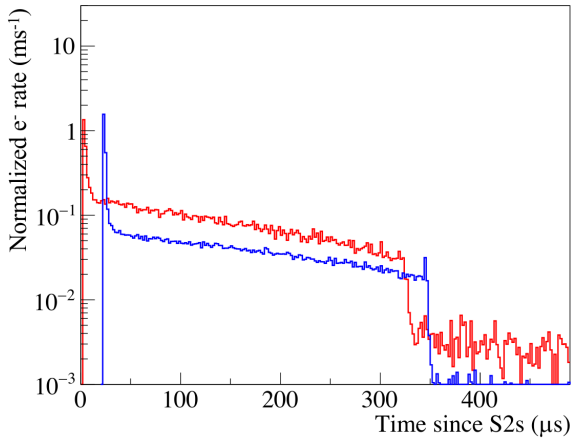

Figure 4.1: The distribution of single electron detection time after thousands of selected ^{83m}Kr-decay S2s at low (red) and high (blue) electron lifetime seen in the LUX experiment. The peaks near 0 and 325 μs are mostly from photoelectric effects on the electrode surfaces, and the continuous distribution in between is from photoionization in the liquid. The blue histogram is offset by $+20$ μs for better visualization. Figure and caption from [59].

The strong time correlation of the initial S2 and the following single electron allows for substantial suppression of single electron events by exploiting a time veto after high energy events of at least one drift-time [59, 66]. In principle, the same holds for a space correlation veto but the position resolution in Xurich II is limited for single electron events, see chapter 5. A space correlation cut could help to reduce single electrons coming from impurities

but it would not help against emissions coming from the grids.

4.2 Extraction and Delayed Emission

Additionally to a delay caused by electronegative impurities, electrons can be delayed by the liquid-gas interface. The liquid-gas interface acts as a potential barrier which the electron has to traverse and the possibility that electrons do not reach the gas phase, especially for low extraction fields, exists. Not emitted electrons cannot continue their drift and thus are no longer accelerated by the external electric field. They will quickly slow down through interactions with the surrounding until they are in thermodynamic equilibrium. If these "thermalized" electrons regain energy they can later be extracted to the gas phase [38, 67]. In reference [59] capillary waves, which may be generated by the xenon flow or bubbles are named a possible mechanism that could extract trapped electrons.

Since the kinetic energy and the z-component of the electron momentum scale with the applied field strength, the extraction probability can be increased by a stronger extraction field. In the XurichII detector, a comparably high extraction field of 10 kV/cm is applied and the correlation between the field strength and the extraction efficiencies suggests that the extraction can be assumed to be 100% [68, 69, 70].

4.3 Grid Emissions

Increasing the separation between cathode, gate and anode, while keeping the electric fields at a constant strength, requires significantly larger voltage biases. Increasing the voltage has historically been difficult for Xenon-TPCs since grid emissions started to appear that limited the electrical performance. Explanations like physical or chemical defects have been proposed, but the exact causes have not been resolved.

It is known that the electric field strengths at the wire surface can reach much higher values than in the bulk part of the liquid and field strengths up to $\mathcal{O}(100\,\mathrm{kV/cm})$ are not uncommon [71, 72]. Even though the field strength on the surface is larger than in the bulk, it is not expected to be high enough to cause electron emissions directly from the wire [73]. The electron potential energy outside the metal surface decreases linearly due to the applied field, and the step potential at the metal-xenon interface is rounded due to the image charge seen by an electron in liquid xenon. This modification of the potential barrier allows conduction electrons near the Fermi level to tunnel into the lower-potential regions of the surrounding liquid xenon. The phenomenon can be described within the framework of Fowler-Nordheim theories and in the original paper from 1928 the following sentence is stated: *This will make the emission begin to be sensible for fields of rather more than* 10^7 *volts/cm* [73]. What exactly the authors mean with *sensible* is not clear and that TPCs with single electron sensitivity can detect electrons at much lower fields is likely. Despite the fields on the surface of the wires being high, they are still orders of magnitudes away from the mentioned value and field emissions alone are not enough to explain localized electron emissions [72, 71]. It has been suggested that corrosion products on the surface of the wire could be the leading cause of the spurious emission, and it has been shown that such imperfections could be greatly decreased with a high-quality chromium oxide layer and acid cleaning of the metal grids[74, 72].

In [59] the single electron emissions were carefully studied but not all emissions show the same behavior and it is very difficult to reproduce them. In some instances, the emissions increase with the electric field and in others, they seem to vanish with increasing field. In total three different types of emissions were registered: localized emitters over a narrow range of fields, impulsive emitters with very high instantaneous rates which can appear and disappear over a short time, and a faint source of emission present at all fields.

4.4 Correlation to Rate of Energy Deposition

A connection between the rate of single electrons and the overall rate of energy depositions was concluded in [75] and is very sensible if the photoelectric effect and the photodetachment of impurities are the leading cause of single electrons. More events cause more scintillation light and more scintillation light causes more single electrons. In figure 4.2 the correlation between the rate of energy depositions due to the ^{37}Ar calibration source and the single electron events is illustrated with data from Xurich II. Shown is the time difference between an initial large S2 and the following single electron in two data sets with a different activity.

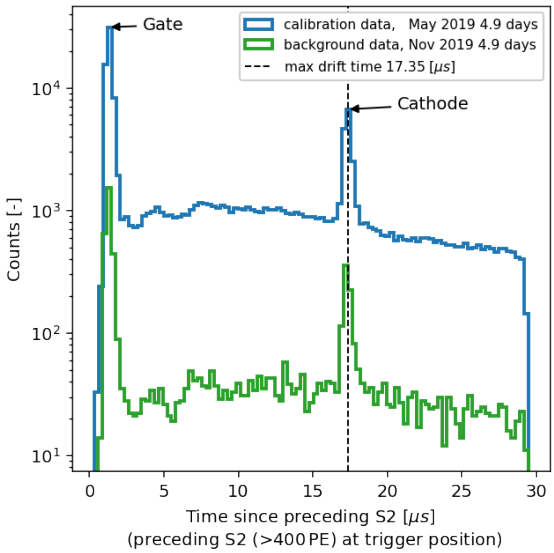

Figure 4.2: Time difference between an initial large S2 and a subsequently following single electron two data sets from the calibration run of Xurich II, one at the beginning of the calibration run (blue) and at the end (green). The maximal time difference is limited by the length of the waveforms (60 μs) and the position of the first S2. In this histogram, the large S2s are required to be in the middle of the waveform, which results in a maximal time difference of 30 μs.

The "calibration data" was measured directly after the injection of ^{37}Ar and the "background data" was measured more than 4 half-lives later. As the following data analysis will focus on the "background data" it has to be mentioned that there is a contribution from the M-shell electron capture of ^{37}Ar, with an energy of 17.5 eV. These decays produce single electrons within the region of interest but an estimation from branching ratios implies that the M-shell contributes only very little, about 1.7%, of the single electron rate.

Summary

The ideal TPC experiment that looks for single to a few electron events has a high extraction field, low backgrounds, high xenon purity and ideally no metal that is exposed to scintillation light. Low backgrounds are usually achieved by going deep underground to shield against the cosmic rays and by screening the materials to remove radiation from the instrumental parts. Going underground is not an option for a search of strongly interacting dark matter, since the overburden can substantially reduce the flux of the incoming dark matter as discussed in section 3.3. The backgrounds in the single to a few electron region are only partially understood and there could be more effects than just the ones mentioned here. It remains to be seen if there are undiscovered effects that play a role as well.

From the mentioned backgrounds, photodetachment is probably the only place where an improvement can be expected as new xenon TPC experiments target higher xenon purity and electron lifetimes beyond one millisecond are expected [76]. Finding an electrode design that allows a high extraction field and zero emissions, is a lot more difficult. Especially since most common metals have a work function around $\sim 4.5\,\mathrm{eV}$ that is below the energy of the xenon scintillation light energy. Specially material selection and dedicated surface treatment can potentially help to further reduce emissions from the grids.

Concerning the following analysis the easiest and most effective reduction of backgrounds probably would have been a data-set from the time before the injection of ^{37}Ar. There the level of activity and with it the rate of single to a few electrons would have been much lower.

Chapter 5

Data Analysis

In this chapter, the data analysis of the Xurich II data is described in detail. The focus of the analysis was to study the single to a few electron region and create an appropriate event selection for the dark matter-electron scattering analysis. It has to be emphasized that the master project was started after data taking and the experiment had been decommissioned, such that no additional experimental data could be gathered during the project. As already has been mentioned, the data set of interest was taken at the end of the calibration run with ^{37}Ar conducted in 2019, see section 2.2.2.

5.1 Data Preparation

The analysis was planned to be based on S2-only events and therefore the information of all the S2s in the waveforms was required. The previously processed data did not contain all the recorded S2s since they were not needed for the calibration. Hence the first step of the project was to repeat the last step of the data processing, in which previously some S2-only events where filtered out. The pulse attribute definitions, the identification algorithm, and the gains were all the same as in [36] and are reviewed in the following.

Pulse Attribute Definitions

Events in the Xurich II detector are recorded in waveforms with a length of 60 μs and the pulse which caused the trigger is placed in the center at 30 μs. In figure 5.1 an example of a waveform with an S1-S2 pair is shown. In this case, the S1 caused the trigger and therefore is placed in the middle of the waveform at 30 μs.

The basic requirement for a pulse to be accounted as of physical origin is the simultaneous detection by the PMT at the bottom and at least one of the SiPMs at the top. Pulses are here defined as a collection of peaks which fulfil this coincidence requirement. If only two SiPMs detected a peak in coincidence, it is discarded because the PMT with its large surface area has the highest probability to detect a light signal. In addition to the coincidence requirement, a pulse issues the trigger if it has a height, seen by the PMT, of at least 7 mV. If a pulse causes the trigger, within 30 μs before and after that pulse everything is saved. In the following the basic pulse properties that are saved in the last step of the processing are listed for S2s and for S1s they are the same.

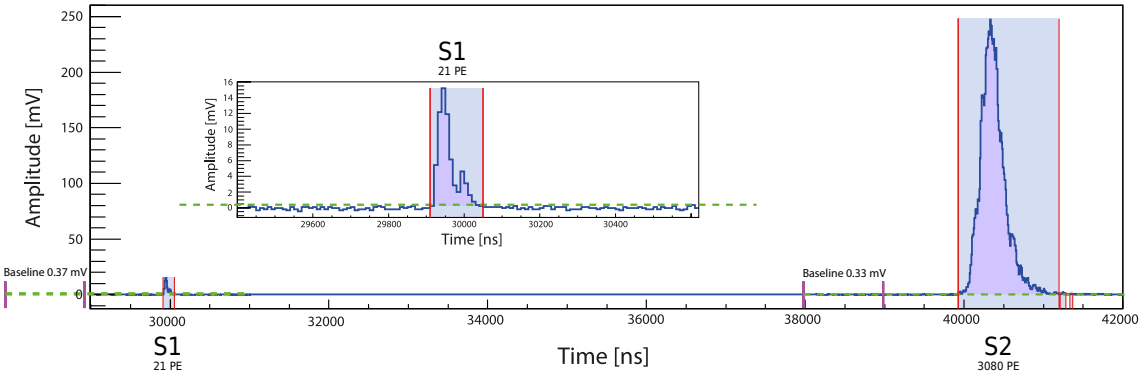

Figure 5.1: Example of a waveform recorded by the PMT. The waveform shows an event of a K-shell capture of ^{37}Ar. The time difference indicates that the event happened in the liquid xenon between the gate and the cathode. The inlet shows the S1 pulse magnified.

The area is defined as:

$$S2_{\text{area}}[\text{PE}] = \text{c}_0 \cdot \left[\frac{\text{A}_{\text{pmt}}}{\text{g}_{\text{pmt}}} + \sum_{\text{i}}^{16} \frac{\text{A}_{\text{sipm,i}}}{\text{g}_{\text{i}}} \right] \qquad \text{c}_0 = \frac{2.25\,\text{V} \cdot 10\,\text{ns}}{\text{q}_{\text{e}} \cdot 2^{14} \cdot 50\,\text{Ohm}} \tag{5.1}$$

with A the area between the signal and the the baseline, c_0 the conversion factor from digitizer counts to PE, and q_e the charge of the electron in Coulomb. c_0 depends on the specific digitizer model (CAEN V1724).

The position is defined:

$$S2_{\text{position pmt}}[10\,ns] = p_{\text{pmt}} \tag{5.2}$$

where p_{pmt} is the position of the maximal height of a pulse. Notice that $[10\,ns]$ is the resolution of the digitizer in time and hence this represents the position in time not in space.

The height is defined as:

$$S2_{\text{height pmt}}[V] = c_1 \cdot h_{\text{pmt}} \tag{5.3}$$

where h_{pmt} is the the highest value of the pulse and $c_1 = \frac{2.25\,V}{2^{14}}$ the conversion to Volt.

The width is defined as :

$$S2_{\text{width pmt}}[10\,ns] = w_{\text{pmt}} \tag{5.4}$$

where w_{pmt} is the width at 10% of the maximal height of the pulse seen by the PMT.

Pulse Identification

The pulse identification algorithm utilizes the fact that S1s have much smaller widths than S2s, which is due to the short decay constant of the xenon scintillation light, (4.3 ± 0.6) ns

and (22.0 ± 1.5) ns for the singlet and triplet states respectively [77]. The pulse identification described in [36] works as follows:

S1 and S2 signals are distinguished by width-based filters, where the filters at the i-th bin is defined as:

$$S1_i = \sum_{i-\frac{w_1}{2}}^{i+\frac{w_1}{2}} A_j \qquad \text{and} \qquad S2_i = \sum_{i-\frac{w_1}{2}}^{i+\frac{w_1}{2}} A_j - S1_i \tag{5.5}$$

A_j is the baseline-subtracted signal at the j-th bin and $w1, w2$ are the two widths. While a maximum summation width of $w1 = 20$ samples contains the entire S1, $w2$ was chosen to be maximum 100 samples. The sums are bounded by the peak integration window to guarantee that it is not summed over a distinct close-by peak. Both filters are evaluated at i being the center of the full width at half maximum of the peak to account for their asymmetric shape. The S2 filter will be zero for an isolated S1-like signal and much larger for an S2. We choose the ratio S2/S1 as discriminator and identify a peak with S2 if this ratio is > 0.2, i.e. if > 20 % more charge is contained within $w2$ than within $w1$.

The width-based approach works well for S1-S2 events as they appear in calibration runs either with ^{37}Ar or ^{83m}Kr [43, 36]. For events with no such a clear structure, for example, small S2s, the accuracy is not known but is attempted to be estimated in chapter 6. A comparison with an accurate simulation or the measurement of a induced signal, for example via the photoelectric effect, could potentially reveal interesting insights.

Position Reconstruction

The location of an S2 pulse in the xy-plane is an important feature of the detector and allows for a fiducialization later in the analysis. In the following, the procedure is described, showing only the formulae for the x-coordinate, the y-coordinate is treated accordingly. The procedure is taken from [36], where more details can be found. In the first step, the position in the x-direction is first calculated as a weighted mean, called the center of gravity approach, with the weights being $S^i_{2\,\text{area}}$ the amount of light seen by the ith SiPM and x_i the center of the ith SiPM.

$$x_{\text{uncorrected}} = \frac{\sum_{i=1}^{16} S^i_{2\,\text{area}}\, x^i_{\text{SiPM}}}{\sum_{i=1}^{16} S^i_{2\,\text{area}}} \tag{5.6}$$

These uncorrected coordinates have a range of $[-10.9, 10.9]$ mm which corresponds to the outer square formed by the centers of the SiPMs. In the following, the coordinates are centered and scaled to a unit square by

$$x_{\text{scaled}} = (x_{\text{uncorrected}} - \Delta_x)/c \qquad \text{with} \quad c = 6.5 \quad \text{and} \quad \Delta_x, \Delta_y = 0 \tag{5.7}$$

In the third step, the coordinates are mapped on a unit circle with

$$x_{\text{mapped}} = c\, x_{\text{scaled}} \sqrt{1 - \frac{1}{2} y_{\text{scaled}}^2} \tag{5.8}$$

After having coordinates on a unit circle they are scaled to the true diameter of the cylindrical TPC ($d_{\text{TPC}} = 31\text{mm}$) with.

$$a = \begin{cases} d_{\text{TPC}}(\frac{1}{2} - \frac{1}{\pi}\arccos(\frac{r_{\text{mapped}}}{5.8})) & \text{if } \frac{r_{\text{mapped}}}{5.8} \leq 1 \\ 15.5\, mm & \text{otherwise, map the event to the TPC wall} \end{cases} \tag{5.9}$$

$$x_{\text{corrected}} = \frac{a}{r_{mapped}} \cdot x_{mapped} \tag{5.10}$$

The position reconstruction algorithm gives a position resolution of $\sim 1.5\,\text{mm}$ in the horizontal plane and was developed for and with the signals from ^{83m}Kr and ^{37}Ar K-shell decays. The scaling in equation 5.7 was not done for the maximal value of x and y but instead the characteristic mesh pattern was used to find optimal scaling. In figure 5.2 the top view of the meshes and the focal points that were used to find the optimal scaling are shown.

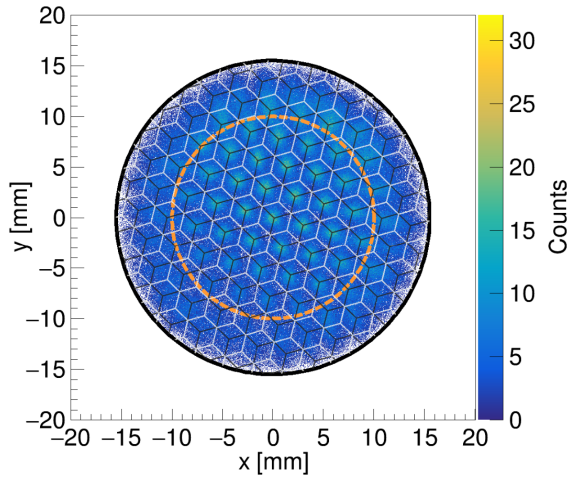

Figure 5.2: Position reconstruction from ^{37}Ar calibration. Shown are the gate mesh in black and anode mesh in white overlayed with the event distribution [36].

A very different situation appears for the distribution of single electron events, shown in figure 5.3. For single electrons, significantly less light is detected and the focal points do not appear. In the case of a single electron, approximately 7 PE are detected by the top array, which is much less than the roughly 1000 PE that are detected for an S2 from a^{37}Ar K-shell event. The small signal creates a much poorer horizontal position resolution for single electron events which is indicated by the points and lines in figure 5.3 that appear when events are only detected by one or two SiPMs.

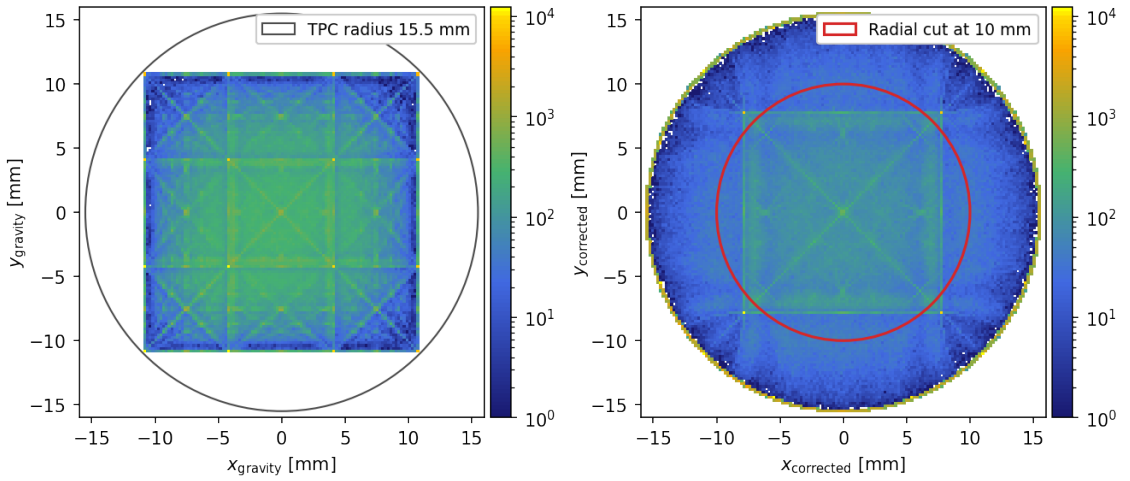

Figure 5.3: Left: Position reconstruction of single electron events computed with the uncorrected center of gravity approach. The bright yellow dots correspond each to a center of a SiPM and reflect the situation when a event was only detected by a single SiPM. The 4 corner SiPMs coincide with the perimeter of the TPC which means, they are partially covered. Right: The result of the position reconstruction algorithm as described in the text for a selection of single electron events.

The right panel in figure 5.3 shows the result of the position reconstruction algorithm and it shows that the features from the center of gravity approach are maintained and enlarged for the innermost part. The linear region of the projection of equation 5.10 defines the radial fiducial volume to be $r \leq 10\,mm$. This is a slightly stronger condition, than the before mentioned coincidence requirement, namely all the pulses within the 10mm radius are seen by at least two SiPMs and the PMT, so a threefold coincidence is required instead of a twofold.

5.2 Peak Splitting Algorithm

To resolve the event topology of ^{83m}Kr, which is another commonly used calibration source, a special peak splitting algorithm was used because the events contain two S1s and S2s in very short succession. To resolve such events nearby pulses are split based on the moving average of 4 bins respectively 2 bins depending on the length of the pulse. A pulse is split if the moving average falls below the individual maximum value and enables two close S1s to be very efficiently distinguished. The splitting algorithm also affects small S2s since it separates even small fluctuations into individual pulses and creates a lot of small, S1 like pulses. In this analysis, where no ^{83m}Kr is used and S1s are not relevant, the splitting is undesired because small S2s can falsely be split into multiple S1s. In figure 5.4, a histogram of the S2-Area is shown for the same data set where the splitting algorithm once turned on (blue curve) and once turned off (green curve). A significant difference in the number of small S2s can be observed. The single electron peak grows about one order of magnitude when the algorithm is turned off. Based on these arguments it was decided to keep the algorithm turned off for this analysis.

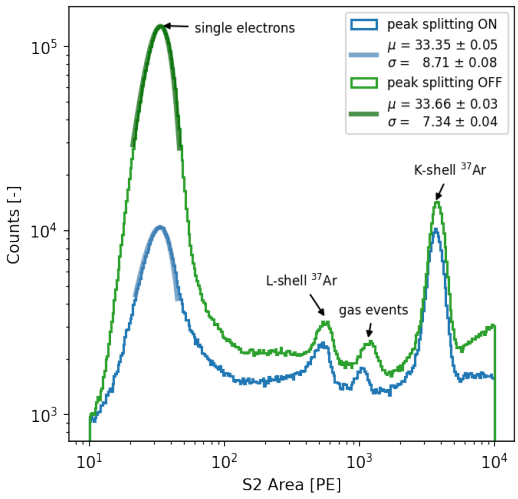

Figure 5.4: S2 Area histogram for the whole background data-set with the peak splitting turned on (blue) and off (green), after applying the noise cuts, which will be discussed later in this chapter. The four prominent peaks are from left to right: the single electron peak (∼35 PE), the L-shell events of ^{37}Ar (∼ 560 PE), gas events (∼1000 PE), and then the K-shell events of ^{37}Ar (∼4200 PE) events.

5.3 Trigger Rate

The ^{37}Ar calibration required a fine tuning of the trigger threshold such that the small S1s could be detected and meaningful S1-S2 pairs were acquired. With the chosen settings a large part of the data showed an unstable trigger rate which is vital for a dark matter search. A changing trigger rate can either come from instrumental sources or from a fluctuation in the rate of physical events. The observed step like behavior, see figure 5.5, between 42 Hz and 26 Hz is indicative for an instrumental issues especially since in previous calibrations with ^{83m}Kr, stable trigger rates with much higher frequency (∼ 140 Hz) were achieved.

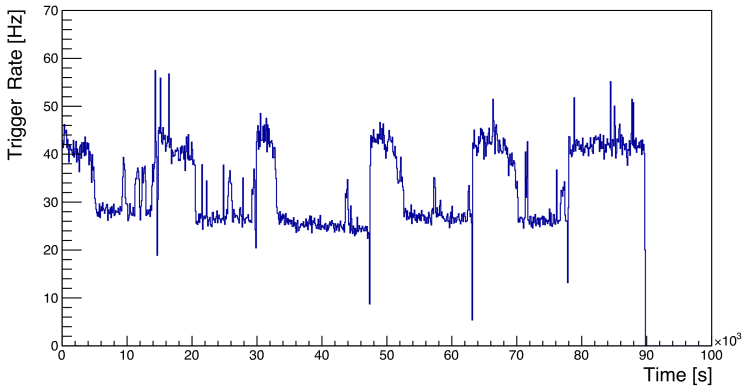

Figure 5.5: Trigger rate measured in 6 consecutive files acquired at the first of November 2019. The rate moves between a higher level around 42 Hz and a lower level of 26 Hz.

The files with an unstable trigger rate had to be removed and the total measurement time of initially 10 days was reduced to 1.3 days of files with a stable trigger rate. For

a calibration, which was the purpose of the experiment, the stability of the trigger rate is not ideal but not a big issue. A possible reason for the unstable trigger rate can be the different attenuator setup that was used in the ^{37}Ar case compared to the more stable setup with ^{83m}Kr. There the PMT signal was attenuated by a factor of 10.

5.4 Differences to Previous Post-Processing

During the last step of the processing, a couple of details emerged that were treated differently and the biggest difference is, that only waveforms with at least one S2 are saved. Additionally, pulses are not paired into S1-S2 events because such a pairing is not possible nor meaningful for S2-only events.

During the length of a pulse that is measured by the PMT, SiPMs often detect multiple peaks that have to be attributed to the same pulse. In the previous version, a small bug was found that caused only the last peak of each SiPM to be saved. This was changed such that all contributions are summed and correctly added to the total. The different amount of light seen by each SiPM affects the position reconstruction in the horizontal plane as the area recorded by each SiPM is the weight in the center of gravity algorithm. This change is especially relevant for the single electron regime where only a small amount of light is detected in the top array.

Another small difference emerged in the coincidence requirement. Previously it was not required for the coincidence that the area of each peak, seen by a SiPM, is positive. This means that pulses, where the SiPMs recorded negative areas, were passing the coincidence requirement. This was changed such that only pulses with a least one positive peak from the SiPM together with the PMT signal fulfill the coincidence requirement.

Two small additional bugs appeared while implementing the position reconstruction algorithm. First, there is an obvious problem if $1 - \frac{1}{2}y^2_{\text{scaled}} < 0$ in equation 5.8, that restricts the input domain to be smaller than then the whole domain, see the red square in the left panel of figure 5.6. The second problem is more subtle and concerns the function in equation 5.10. If the mapping function is evaluated along the direction $\vec{a}$, indicated with the red arrow in the left panel of 5.6, the blue curve in figure the right panel of figure 5.6 is returned. As it is shown, events that have a radial position of $r_{gravity} \approx 12.5\,\text{mm}$ are falsely mapped into the center of the TPC. To solve this issue, equation 5.10 can be modified in the following way.

$$a = \begin{cases} d_{\text{TPC}} \left[\frac{1}{2} - \frac{1}{\pi} \cdot \arccos(\frac{r_{\text{mapped}}}{5.8})\right] & \text{if } \frac{r_{\text{mapped}}}{5.8} \leq 1 \\ 15.5\,mm & \text{if } \frac{r_{\text{mapped}}}{5.8} > 1 \text{ or } \mathbf{r_{gravity} > 7\,\text{mm}} \end{cases} \tag{5.11}$$

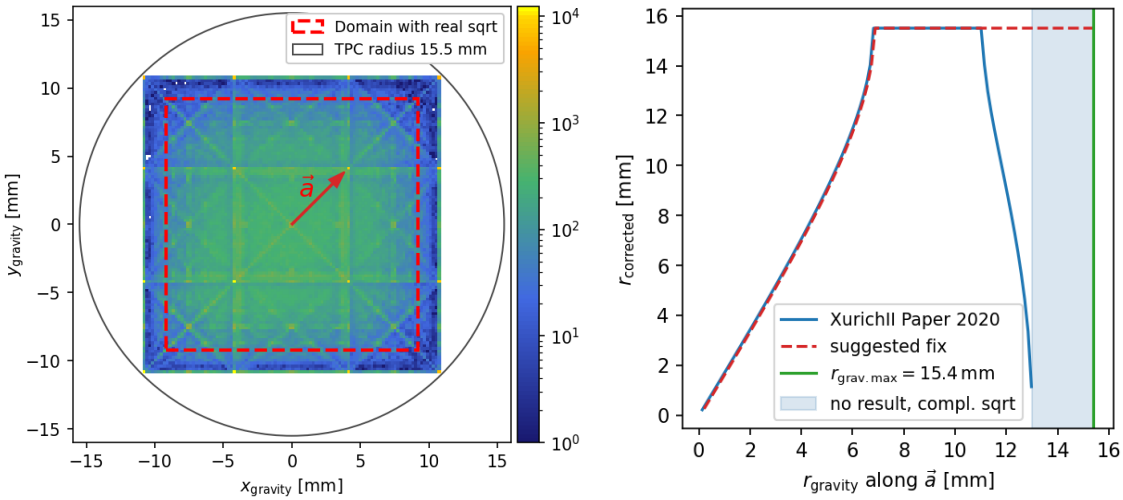

Figure 5.6: Right: The center of gravity position calculation for single electron events shown together with the TPCs perimeter (black) and the direction in which the issue in the position reconstruction occrued (red arrow). Left: Result of the radial position reconstruction along $\vec{a}$ and the three other corners of the SiPM array.

The bug in the position reconstruction algorithm only affected a small portion ($\sim 5\%$) of all the events because it only occurred for events in one of the 4 corners. All bugs were reported, fixed and the two post-processing versions provide equivalent outputs.

5.5 Noise Reduction

Up to the post-processing, the stage where physical events were constructed, no filter or method to eliminate noisy waveforms was applied. The fact that such a treatment is necessary is visible in the left panel of figure 5.7, where a histogram of the number of observed peaks in each waveform is shown. The high number of peaks per waveform is indicative that there are instabilities coming from the electronics or the photosensors. These unstable conditions were observed often directly after an event that saturated the data acquisition system (DAQ) and consequently a high number of peaks appear in these waveforms. These peaks are very unlikely of physical nature because often baseline-jumps appear, see right the right panel of figure 5.7 for an example.

The instabilities suggest dead times, where no detection of physical interactions is possible, and in principle that is not a problem when handled correctly. First of all the noise-related waveforms have to be removed because they are processed as normal events and create fake signals that should not be considered. In the second step, the measurement time needs to be corrected by this dead time. Since the experiment is operating in a regime where the physics reach is most probably limited by backgrounds instead of a too small exposure, the goal is to remove everything that is non-physical and concerns about a small exposure have a secondary priority.

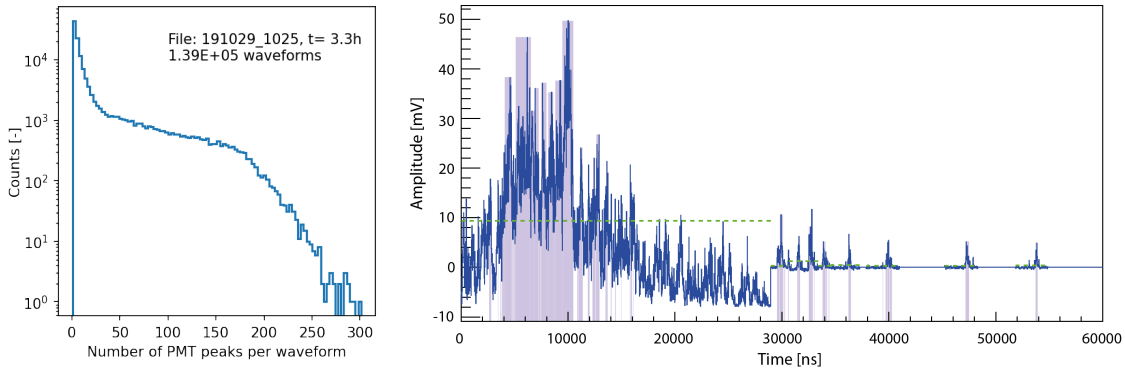

Figure 5.7: Left: Example histogram of the number of peaks seen by the PMT. Notice the difference between the definition of peaks and pulses, which means a large number of peaks is not necessarily seen by all the photosensors and can indicate an issue with the electronics. Right: A waveform recorded by the PMT that includes noise and a baseline-jump. The noise cuts that will be discussed in the following aim to remove such waveforms.

Due to the occasionally high number of peaks observed by the PMT, a cut based on this variable was developed. As a reference for a meaningful number of peaks seen by the PMT, K-shell events from ^{37}Ar were used. In these events, selected as described in [36], an average number of 8 peaks is seen by the PMT and it was decided to use an upper limit of 15 peaks. This cut keeps 92 % of all the K-shell electron capture events and since no S1 is expected for S2-only events it should have an even smaller impact on the events of interest. Pulses with a height larger than $1.6\,V$ saturate the fan-in/fan-out module and have to be removed. Together with the waveform containing the saturated pulse, waveforms directly afterwards are also removed. This was done based on the observation that saturating pulses often cause instabilities and baseline-jumps in the following waveform. Another noise indicator are pulses that are very wide but do not saturate the PMT. It was decided to remove all waveforms which have a pulse that has a width more than three times ($> 3\,\mu$s) as wide as the width of a K-shell S2s, which usually have width of $0.4 - 0.8\,\mu$s[1]. In total these observations lead to the following three noise cuts.

Remove waveforms with the following features:	Removed w.r.t all waveforms containing an S2
i) The waveform follows directly a waveform that includes a saturating pulse.	25.4 %
ii) The PMT recorded more than 15 peaks.	20.9 %
iii) The PMT recorded a pulse wider than $3\,\mu$s.	2.2 %
Removed in total :	48.5 %

[1]Notice that the very wide pulses are not part of the region of interest. Pulses with a width larger than $3\,\mu$s have a area that is larger than the upper limit, as will be discussed in the following.

5.6 Event Selection

The goal of the event selection is to select events that have no prompt scintillation light (S1) but secondary scintillation (S2). Meaning that if a low energetic initial interaction creates a small number of photons and electrons, only the electrons will be detected. The dark matter-electron scattering introduced in chapter 3 creates a signal in this regime, where initial recoils are low energetic and the created light falls below the detection threshold [2]. The event selection, therefore, focuses on the selection of S2s that do not have an S1 and fulfill none of the known structures that are related to backgrounds. In figure 5.8 an overview of all the used S2 features is shown before the selection and after removing all of the noise-related waveforms.

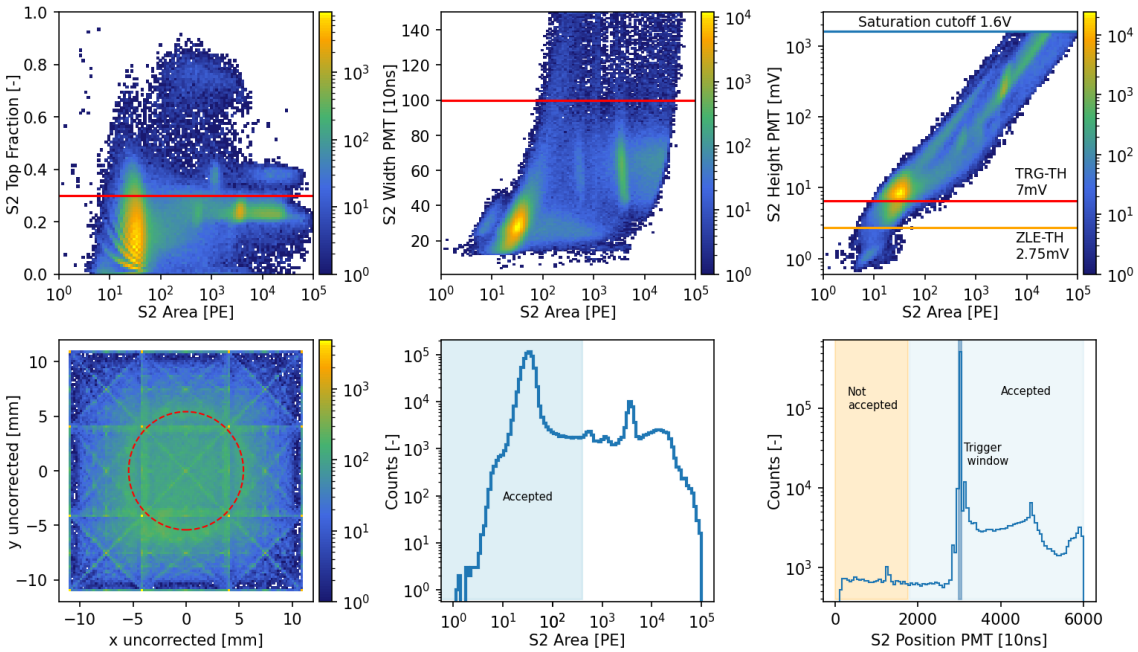

Figure 5.8: Overview of the S2 features. Shown are 2D histograms of S2 area fraction top, S2 width and S2 height versus the S2 area, a 2D histogram of the x-y distribution, a histogram of the S2 area, and a histogram of the S2 position after applying the noise cuts and before the event selection. The red lines represent the event selection discussed in the text.

The maximal time by which S1 and S2 can be physically connected, is the time it takes to drift an electron from the cathode to the gas phase[3]. This maximal drift time Δt_{max} can be inferred from figure 4.2 and has a value of 17.35 μs. This means, for the selection, that an S2 should not have any S1 in this time ahead, see waveform 1) in figure 5.9. Candidate S2s additionally should have pulse features that are in agreement with signals that are known to come from physical sources.

[2]The energy detection threshold of the S1s lies in between 270 eV and 2.8 keV and are indicated by the absence of the S1 at 270 eV (L-shell decay of ^{37}Ar) and by the presence at 2.8 keV (K-shell decay of ^{37}Ar)

[3]The term "drifting" understates a bit the speed (1′786 m/s) that the electrons have in the liquid xenon at a field of 968 V/cm.

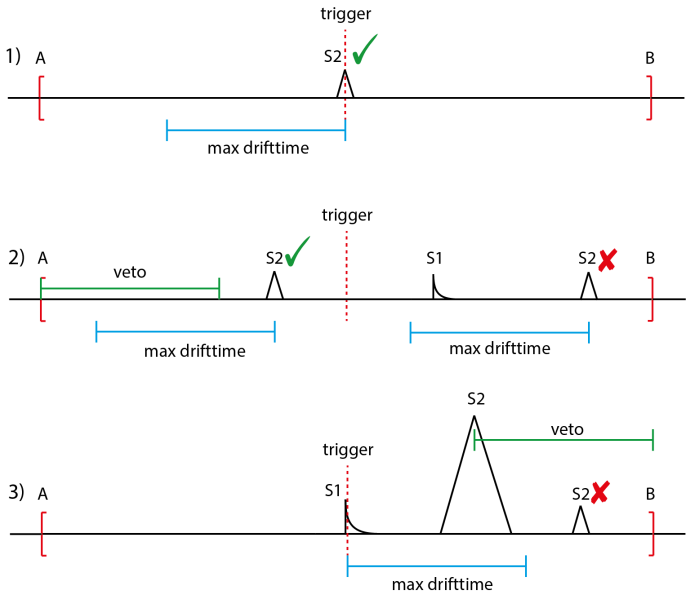

Figure 5.9: Schematic waveforms showing in 1) the ideal case with a small lone S2 at the trigger position within the waveform from A to B, in 2) a small lone S2 and an S1-S2 pair and in 3) the structure of background events from either photo-detachment or the photoelectric effect caused by the large S2. Distances are drawn to scale but the pulse shapes and sizes are exaggerated.

The main background that should be avoided are events from photodetachment and the photo-electric effect on the metal surfaces. The two effects, as discussed in section 4.1, are usually observed as a succession of pulses with one main S1-S2 pair but with one or more small S2s that follow the main S2. Due to the time structure, it was decided to put a time veto after large S2s such that none of the small S2s afterward are selected, see waveform 3) in figure 5.9. As discussed in section 4.1, a time veto after a large S2 of at least one drift time Δt_{max} is required to remove this background effectively. Since the large S2 can be saved at different locations in the waveform, this cut is of variable length but ensures the time veto of at least one drift time Δt_{max}. This can be seen as a relatively simple and conservative solution because the basic contribution of single electrons is removed but all the events that follow with a larger time delay are accepted. The initial motivation for this cut came from [59] where it was suggested to remove the main contribution of single electrons with such a cut.

Because small S1s can easily be missed by the trigger, which happens even for the relative prominent K-shell events from ^{37}Ar, a time veto is put at the beginning of each waveform to ensure there is no S1 in front of the S2, see waveform 2) in figure 5.9. The time vetos reduce the total exposure and have to be taken into account.

Even though the data set was taken more than four half-lives after the injection of the ^{37}Ar, decays via L and K-shell electron capture are still visible in the data, see figure 5.4 and 5.10. The L-shell decays create a natural limit for the analysis because these events appear as well as S2-only events and should not be considered in the analysis. To minimize the number of L-shell events contained in the region of interest, it was decided to set the upper

limit of the analysis to be 400 PE, 2.5 σ away from the L-shell peak, which corresponds roughly to 11 extracted electrons from the liquid to the gas interface. S2 pulses that are below this value are in the following called "small" and the ones larger are called "large" pulses.

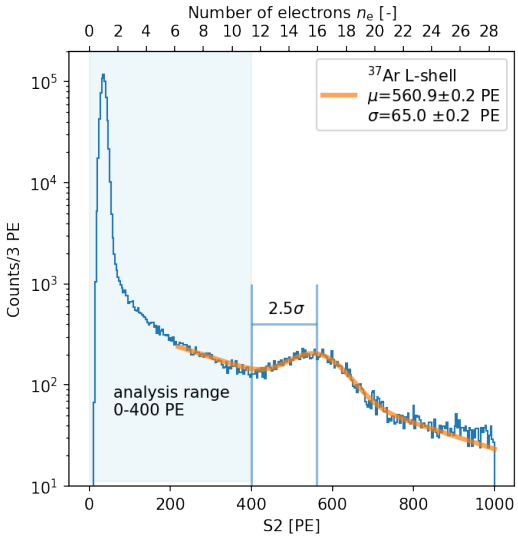

Figure 5.10: Area histogram of all S2-only pulses within the background data set, fitted with the sum of a Gaussian and an exponential function (orange line) in order to find the mean L-shell signal from ^{37}Ar. Events were selected by the selection rules discussed in this chapter but with the upper limit above the L-shell such that its position can be studied.

Cut	Reason	Condition	Passing w.r.t small S2s
small S2s	L-shell at $\sim$ 560 PE	area $<$ 400 PE	100.0 %
no S1	S2-only expected	no S1 in Δt_{max}	19.0 %
not in the beginning	ensure no S1	Δt_{max} after the beginning of the WF	97.0 %
not after a large S2	background mitigation	not after a large S2 (until end of WF)	27.8 %
fiducialization	no wall events	$r_{corr.} < 10$ mm	32.2 %
top fraction	no gas events	top fraction < 0.29	95.2 %
height	must pass the trigger	height PMT > 7 mV	84.0 %
width	physical origin	width PMT $< 1\,\mu$s	99.5 %
Total			18.7 %

Table 5.1: Summary event selection as discussed in the text. The passing percentage of a specific cut is calculated with respect to all the small S2s present in the data and by only considering the specific cut.

Next to the mentioned requirements, the event selection should focus on S2s that originate from physical interactions in the bulk of the liquid xenon. This can to some extend be ensured by the selection that is discussed in the following. However, one has to keep in mind that an S2-only analysis always lacks the information from the S1 and therefore the depth of an event in the TPC. Even though the fiducialization in the z-direction is not possible, a radial fiducialization is possible thanks to the SiPM array and the position reconstruction algorithm. The maximal radius $r_{corrected}$ up to which the position reconstruction is fairly linear is 10 mm, and candidate pulses need to happen within that radius. Additionally, S2s should not stem from interactions in the gas phase, which can be handled with the *area fraction top*, the ratio of light seen by the top array divided by the total measured light. The cut value for the area fraction top was inferred from K-shell signal, see upper left panel in figure 5.8, an set to 0.29. Moreover, the pulses should have a large enough height to issue the trigger (> 7 mV) and a reasonable width ($< 1\,\mu s$). In table 5.1 the here discussed event selection is summarized including all the details.

In figure 5.11 the pulse features of the selected events are shown and in each of the shown variables (area, height, width, are fraction top, etc), a cut is applied. In the S2 area histogram (lower center panel of figure 5.11) it is noticeable that there are almost exclusively single electron events and no clear contribution from two or more electrons. In the S2 position histogram, one can see that the majority of the pulses are recorded at the trigger position meaning that there has not been a large S2 for at least $1.5\,\Delta t_{\max}$. Additionally there is no other S2 present in the waveform than the one selected in 95% of the waveforms.

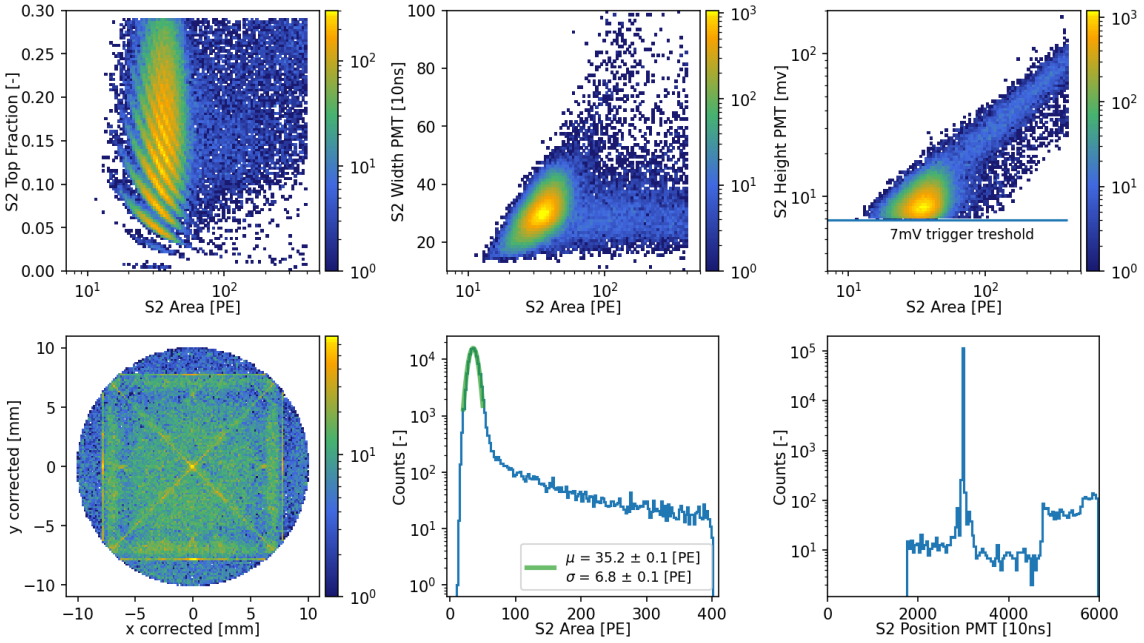

Figure 5.11: Features of selected S2s. Shown are 2D histograms of S2 area fraction top, S2 width and S2 height versus the S2 area, the x-y distribution, the S2 area and the S2 position histogram.

5.7 Hot Spot

During the data analysis, a significant increase of events in one region of the detector was found during short periods of time, see figure 5.12. This excess is not visible in the lower-left panel in figure 5.11 because the single electron contribution ($\sim$ 35 PE) dominates the distribution and the signals were detected with larger areas (50-400 PE). This "hot spot", which contained S2-only events is of unknown origin but the observation matches the description of so called impulsive emitters in [72]. The detected "hot spot" contains events with surprisingly many electrons, up to 10 times more than previously reported [72]. Similar emissions are discussed in section 4.4 but here the goal to remove those signals from the analysis. As the pulses of the hot spot emerge localized in time and space, there are two different options to remove it, with a time cut or fiducializing more. In the first panel of figure 5.13 the "hot spot", as part of the event selection, is shown, In the following panels to the right the outcome of the removal, with either a time or a space cut, is shown. As both cuts remove the "hot spot" efficiently and cause a similar reduction of exposure, it was decided to consider only one of the two cuts and use the different results as a systematic uncertainty.

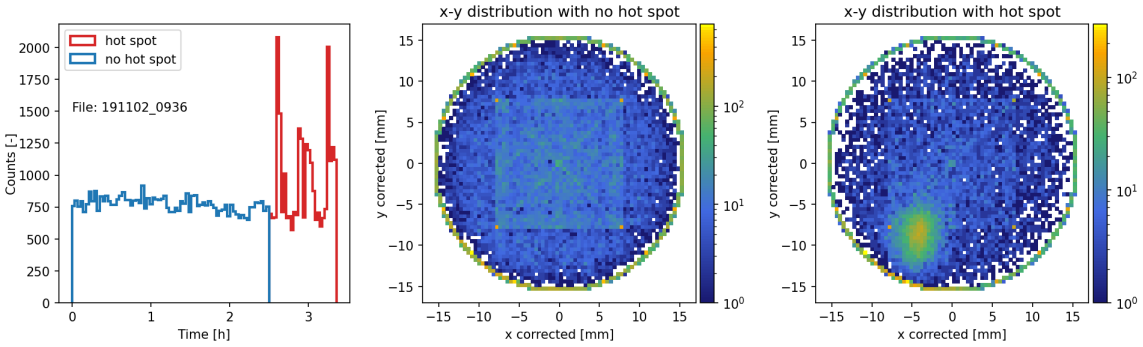

Figure 5.12: Time histogram and x-y distribution of a measurement including the "hot spot". The time histogram shows a clear increase of events (red line) around 2.5 h and in the x-y distribution (third panel) a very localized emission is visible.

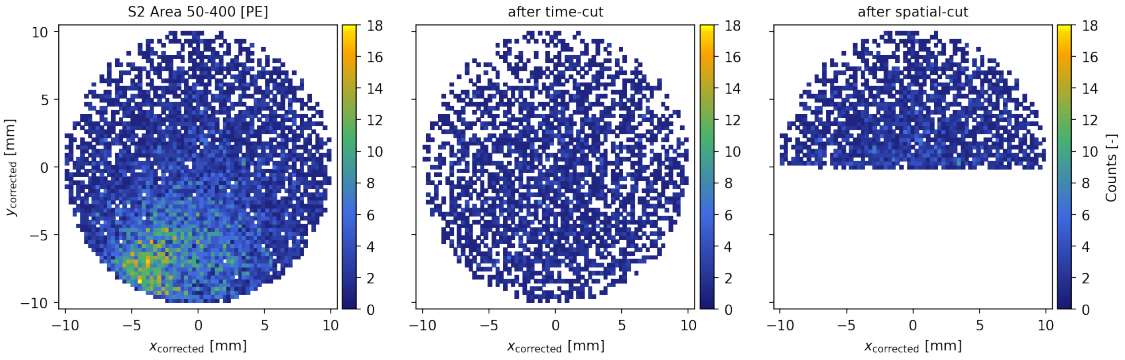

Figure 5.13: Shown are the x-y distribution of events with 50-400 PE that are part of the event selection. In the left panel the "hot spot" is shown and in the middle and right the outcome of the time and space cut. The "hot spot" is effectively removed by either of the two cuts.

5.8 Exposure

To compute the rate of the observed events in the given time and target mass, the measurement time T and the mass M of the experiment have to be known. The mass M of the cylindrical target volume is computed as $M = \rho V = \rho r^2 \pi h = 24.5\,\mathrm{g}$ [36] and the measurement time T is computed as the sum of the 10 measurement files t_i, minus all time that was removed due to vetos or cuts. First, the noise cuts remove fraction f of the total number of waveforms n_{tot} with length t_{wave} and then the two time vetos remove from remaining waveforms $(1-f)n_{tot}$ one drift time Δt_{max} at the beginning. The variable time veto removes the remaining time $t_{k,rest}$ after the kth large $\mathrm{S2}_k$ until the end of the waveform. In total this account to the following

$$T = (\sum_{i=1}^{10} t_i) - f n_{\mathrm{tot}} t_{\mathrm{wave}} - (1-f) n_{\mathrm{tot}} \Delta t_{max} - \sum_{k}^{n_{\mathrm{large\ S2}}} t_{k,\mathrm{rest}}$$

The cuts to remove the "hot spot" further reduce the exposure and in one case the mass M is halved whereas in the other case more time is removed from the exposure. Both cuts reduce the exposure by roughly a factor of 2 and the total exposure accounts to $M = 24.5\,g$ and $T = 0.62\,\mathrm{days}$.

5.9 Result and Discussion

The main result from this chapter is the event rate of small lone S2s that are not correlated to either an S1 or a large S2. This result is shown in the figure 5.14. The left panel shows a histogram of the S2 area with a fine binning and the right shows the number of events normalized by the exposure, binned into n_e the number of electrons.

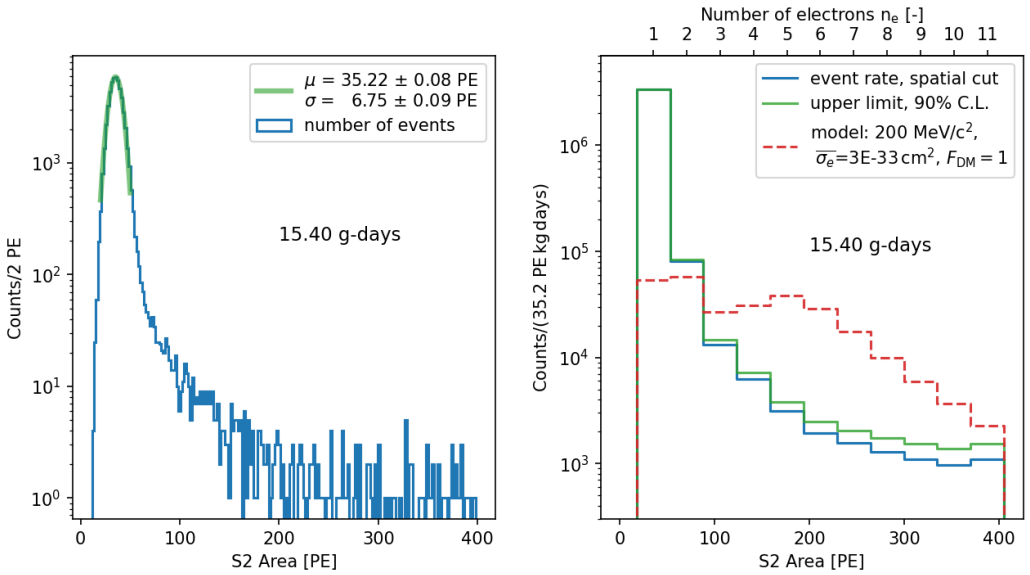

Figure 5.14: Left: S2 area histogram of all lone S2 selected as described in text including the space cut for the "hot spot" removal. Right: The observed rate of S2 (blue line) inferred from the histogram in the left. The rate is shown as a function of area and number of electrons n_e and additionally the upper bound of the confidence interval (green line) and an example signal model (red-dashed line) are shown.

The single electron events are clearly the most abundant and the rate drops off very quickly for events where more electrons are created. The smallest amount of events is seen for 10 electrons, which are seen more than thousand times less often than events with only one electron. In the right panel of figure 5.14 also the hypothetical signature of dark matter interacting via a heavy mediator with a cross section $\bar{\sigma}_e = 3 \times 10^{-33}\,\mathrm{cm}^2$ and a mass $m_\chi = 200\,\mathrm{MeV/c}^2$ is shown.

As the observed number of events and the rate are the result of a Poisson counting experiment [4], which inherently fluctuates, a confidence interval needs to be used for a comparison between the observed and expected number of events. The upper limit of a confidence interval, for n observed events and a confidence level α_{up} is calculated as:

$$\mu_{\mathrm{up}} = \frac{1}{2} F^{-1}_{\chi^2}(1 - \alpha_{\mathrm{up}}; 2(n+1))$$

where $F^{-1}_{\chi^2}$ is the quantile function of the χ^2 distribution [78]. The last topic which has to be studied before conclusions about models can be drawn are the efficiencies but first, a few caveats concerning technical details from this chapter will be mentioned.

5.10 Caveats

The first topic that needs a word of caution is the topic of pulse identification. The algorithm is based on empirical observations that focused on the width of S1s [36]. The pulse identification was not developed for small S2s and there exists no discrimination between real pulses and noise, nor a cross-check to simulations. This means that there could be a lot of pulses that are noise-related and/or misidentified. In the next chapter, an attempt to quantify the missidentification probability will be made but even if a very accurate description is found, there exist a case where the discrimination between real and noise-related pulses can become an issue. If for example a noise-related pulse is labeled as S1 and it is placed before a real S2, the S2 would not be selected due to the no-S1 requirement.

The second topic that potentially introduces a bias is the exposure. The calculation of the exposure relies on the assumption that next to the noise-related waveforms no dead-time of the experiment exists. This is likely an overestimation of the experiment's capabilities but no qualitative statement can be made without looking deeper into the topic. A technical difficulty that is related to the exposure is the length of the waveforms ($60\,\mu s$). With the given trigger rate of 42 Hz, only a tiny part (0.252 %) of the whole measurement time is saved and therefore an estimation of the dead time is difficult.

Next, a few words about longer veto times should be said. Of course, longer veto times after large S2s are possible to implement but ideally, longer waveforms would have been acquired for that. The unrecorded time between waveforms creates a period where it can only be guessed what happened and more detailed studies had to be skipped due to limited

[4] The Poisson distribution describes the probability to measure a given number of events that occur in a fixed interval of time or space if events happen with a known constant rate and independently of the time since the last event.

project time [5]. Longer delay times describe a situation where some mechanism connects an initial interaction and the delayed emission over a time that can greatly exceed the maximal drift time. The mechanisms usually are believed to be the trapping of electrons at the liquid-gas interface or the attachment of electrons to impurities. In XurichII a relatively high extraction field suggests an extraction efficiency of 100% and every electron is assumed to be extracted immediately. Hence longer delay times are only possible if impurities with the electron attached are stable enough or there exist a yet unknown mechanism. The topic of delayed single electron emission is a current research topic, see for example [79, 66, 59], and maybe in the future improved understanding and/or more elaborate techniques allow a better background discrimination.

On the experimental level, the short waveforms complicate the situation with longer time vetos a bit. The poor distinction between noise and S1 creates a lot of artificial S1s, especially after a large S2. Such signals are mostly non-physical but they complicate the interpretation a lot. The question is how to distinguish between a delayed emissions of an S2 and a new S1-S2 pair if there are a lot of noise-related signals. To resolve this issue better discrimination between physical pulses and noise is required.

[5] If longer time vetos want to be studied, the post-processed data files that were created for this project are not suited for such an analysis because only waveforms that include S2s were processed and one has to make sure nothing happens between the initial interaction and the delayed emission.

Chapter 6

Efficiencies

In order to ensure a meaningful comparison between experiment and theory, the efficiency by which the target signals are detected needs to be known. Finding these efficiencies requires an excellent understanding of the experiment and usually repeated measurements or simulations are the way to determine them. Neither of the two ways were accessible at the time of the project and alternative data-driven approaches had to be developed.

It is important that theoretical models start with the calculation in terms of the recoil energy of the electron and the subsequent creation of additional electrons is modeled, as described in section 3.2. The theory, therefore, predicts a number of free electrons in the liquid, and detector-specific effects like the amplification in the gas phase need to be added by the experimentalists. In this chapter, the amplification and the overall efficiency of the experiment will be discussed such that they can be applied to the theoretical models. Complex detector response models, as in [29], which add corrections due to charge loss and additional effects were not implemented.

6.1 Pulse Identification Efficiency

The probability to identify a small S2 correctly after it is detected is determined using a geometrical characterization of the target signals. As an indicative geometrical factor, the ratio of height over width (HoW) was found to give a useful handle to distinguish small S2s from small S1s. The HoW of single electrons pulses is Landau distributed and has a most probable value (MPV) of 2.200 ± 0.002, whereas the HoW of S1s are also Landau distributed but with a MPV of 1.380 ± 0.004, see figure 6.1. Single electron events can therefore be selected by selecting pulses with a certain HoW and by counting through the whole set of pulses, it is possible to quantify how many pulses are labeled correctly. The method is based on the assumption that all the peaks are identified and that the geometrical factor is unique for the target set of pulses. The assumption of uniqueness is not perfectly fulfilled because the S1 Landau distribution has a relatively large tail but the contribution from the S1 distributions tail is negligible compared to the number of pulses close to S2s MPV. By selecting a clean population of single electrons (MPV $\pm 10\%$), the misidentification in the set of all small pulses can be evaluated as a function of area and this yields the identification efficiency (green curve) in the right panel of figure 6.2. The statistical errors are increase with S2 area because the number of events away from the single electron peak is decreasing quickly.

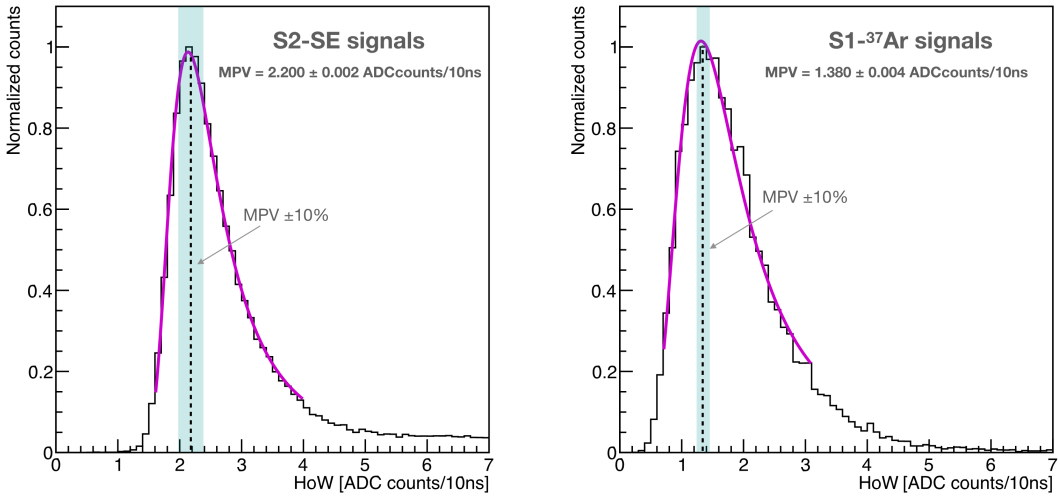

Figure 6.1: Height over width ration (HoW) measured by the PMT for a selection of single electron events (left panel) and S1 signals from the ^{37}Ar K-shell decay (right panel) including fits with Landau distributions. The light blue area around (±10%) the two MPVs indicates the HoW of the signals used in the derivation of the efficiencies.

6.2 Trigger Efficiency

The trigger settings in the Xurich II detector were configured according to the used calibration source and the "background data" had the same trigger settings as the rest of the ^{37}Ar calibration run. The data acquisition and trigger system work in the following way.

The raw data is digitized by three 8-channel CAEN V1724 modules connected in a daisy chain, each with a 100 MHz sampling rate (10 ns samples) and 14-bit resolution at 2.25 V dynamic range. The pre-amplified SiPM signals are fed directly to the Flash ADCs. The PMT signal is not attenuated for ^{37}Ar, then sent to the digitizers. After passing through a CAEN 625 fan-in/fan-out module the trigger is generated by a CAEN N840 leading edge discriminator based on the PMT signal. For ^{37}Ar, we trigger on 7 mV of the raw PMT signal corresponding to approximately > 4-5 PE. [36]

As explained above, the trigger was set up with a discriminator module that triggered on the height of the PMT signal. In particular, the trigger value was set to the height of 7 mV of the PMT signal. This means that the trigger efficiency curve, as a function of the PMT signal height, is expected to follow a Heaviside function with a step at 7 mV. In the left panel of figure 6.2, the density distribution of untriggered and triggered pulses is compared and the step function can qualitatively be confirmed. The selection of the untriggered pulses is possible due to the 30 μs that are saved forward and backward around the trigger position. The untriggered pulses (blue) were found before the trigger position and consequently, the trigger did not catch them.

The main difficulty with the result form the left panel of figure 6.2 is the fact that the efficiency curve is not known as a function of the area and there is no direct conversion between the two features. On a large scale, the height and area correlate but for the single

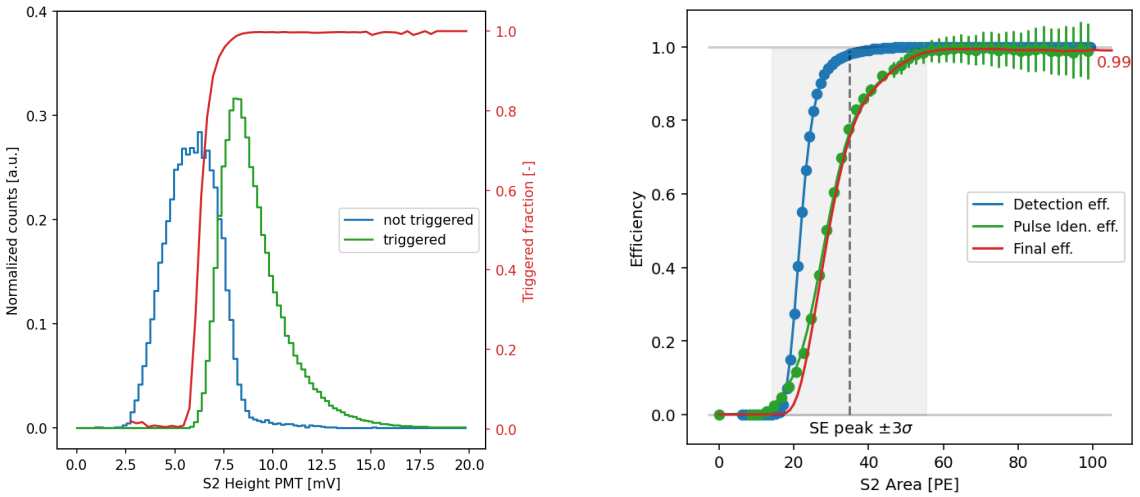

Figure 6.2: Left: The density of the PMT height distribution of triggered (green) and untriggered (blue) signals are shown together with the trigger fraction (red) as a function of height. Right: Efficiencies as a function of S2 area determined as described in the text. The dashed vertical line and the light grey region show the position $\mu \pm 3\sigma$ of the single electron peak.

electron population a considerable variation is observed, see the blob in the upper right panel of figure 5.11. This means a data-driven approach for the conversion had to be developed and will be discussed below.

The relationship between height and area is on a geometrical level intuitive when the width of a signal is constant. For signals in the experiment, the situation is unfortunately not as easy because the ratio between width and height can vary greatly for the different signals. To be sure that the conversion between height and area respects the features of the target pulses, small lone S2s, the conversion had to be adapted for those target signals. The conversion of height to area with a selection of target signals causes the resulting efficiency not to be of general character but of individual, for the analysis under consideration. Hence the name *single electron detection efficiency* is used instead of trigger efficiency.

Selecting a clean population of single electron events is done as before using the HoW ratio and a selection of ±10% around the MPV. With this the conversion from height to area can be achieved in the following fashion. The idea is to loop through all the pulses and apply the height based trigger efficiency, from the left panel in figure 6.2, to the single electron population. The procedure can be interpreted similarly to drawing random numbers from a probability distribution but here the selection of a pulse according to its height and the efficiency curve is the probabilistic step. In the described fashion a set of selected and not selected pulses is created and the conversion from height to area is now trivial because both features are known for each pulse. The procedure results in the single electron detection efficiency (blue curve) shown in the right panel figure 6.2.

6.3 Application to Signal Model

With the efficiencies as a function of area (PE) and the knowledge of the amplification from the left panel in figure 5.14, the detector specifics can be included in the signal model. The rate per electron $\mathrm{dR/dn_e}$ gets transformed to dR/dPE by using the fact that single electron events create a Gaussian distribution of photoelectrons with a mean $\mu_0 = 35.2\,\mathrm{PE}$ and $\sigma_0 = 6.9\,\mathrm{PE}$, whereas an event with i electrons create Gaussian distributions with $\mu_i = i\mu_0$ and $\sigma_i = \sqrt{i}\sigma_0$ respectively.

$$\frac{dR}{dn_e} \rightarrow \frac{dR}{d\mathrm{PE}} \times \varepsilon_{\mathrm{trigger}}(\mathrm{PE}) \times \varepsilon_{\mathrm{ID}}(\mathrm{PE}) \rightarrow \frac{dR}{dn_e} \tag{6.1}$$

The transformation from $\mathrm{dR/dn_e}$ to dR/dPE simulates the amplification in the gas phase and the rate dR/dPE represents the signal before the detection. After the rate is multiplied with the efficiencies ($\varepsilon_{\mathrm{trigger}}$ and $\varepsilon_{\mathrm{ID}}$) and is re-binned into number of electrons n_e, a comparison to the measurement is possible. In the left panel of figure 6.3 the overall effect of the procedure on the signal model is shown and it can be observed to mainly affect the single electron peak. The overlapping Gaussian distributions (grey lines) cause a small smearing, meaning some events of the Gaussian tails are attributed to the neighboring bin.

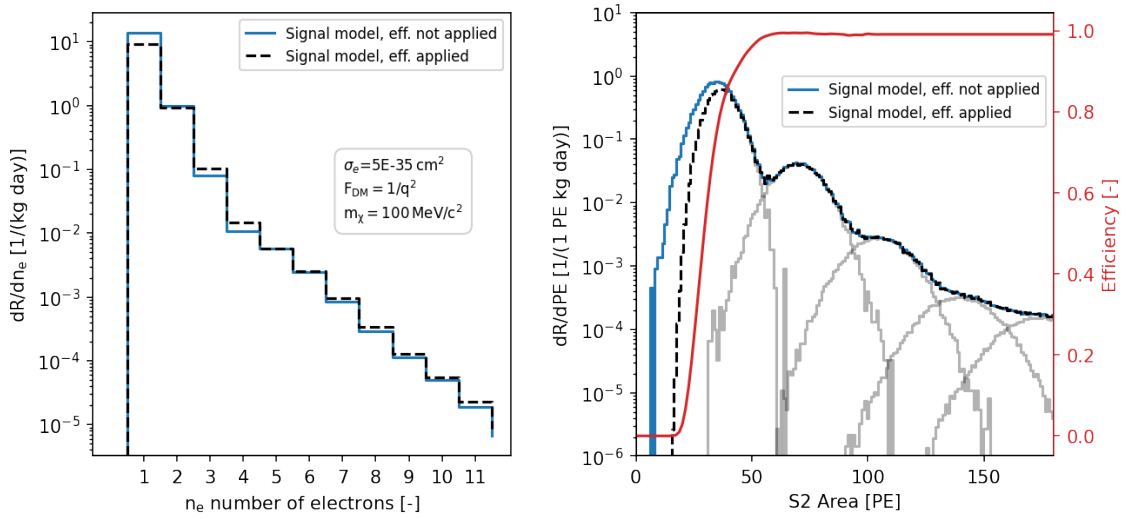

Figure 6.3: Left: A signal model for a dark matter with m_χ=100 MeV/c^2, F_{DM}=$1/q^2$ and $\bar{\sigma}_e$=5×10^{-35}cm^2 before (blue) and after (black-dashed) considering the amplification and the efficiencies described in the text. Right: The signal model from the left transformed to PE, including the final efficiency (red), the individual contributions from the first 5 bins (1-5 e^-, grey) and the sum before (blue) and after applying the efficiency (black dashed).

It must be emphasized that the data-driven approaches are not flawless but nonetheless resembles the best available knowledge and will be used in the following. Improvements can potentially be made with a better understanding of the shape and size of small S2s. Experiments utilizing the photoelectric effect to create small S2s or simulations are viable options to gain more insights about this.

Chapter 7

Results and Conclusion

Since there exists no background model for the region of interest and the signal model can be corrected with the efficiencies from the last chapter, a comparison between experiment and theory is now possible. Exclusion bounds are determined requiring the resulting signal model to be less than the data at 90% confidence level in each bin, see figure 5.14 for the comparison of the rates from model and the data. The signal models which do not pass this requirement are excluded and are part of the blue exclusion region in figure 7.1.

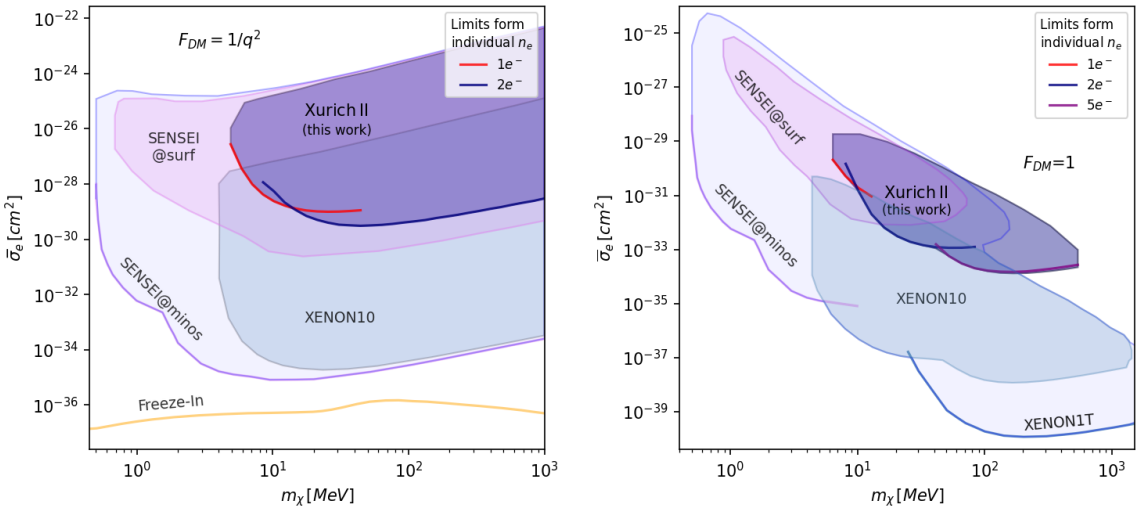

(a) ultralight mediator

(b) heavy mediator

Figure 7.1: Exclusion regions at 90% confidence level from Xurich II (blue region) and bounds from the individual number of electrons shown together with current constraints from SENSEI, XENON10 and XENON1T [33, 27, 29]. Shown are the exclusion bounds for two different dark matter-electron interactions in (a) the ultralight mediator case (b) the case with a heavy mediator. The "hot spot" was removed from the data with a spatial cut.

In the case of the ultralight mediator all excluded models were previously excluded either by SENSEI or XENON10. However, in the heavy mediator case, there is a region where no other experiment was able to constrain sub-GeV dark matter before. Models with either a very weak interaction, producing only very little signal, or models that are strongly atten-

uated remain unconstrained (white area). This causes the constrained area in the ($\bar{\sigma}_e$,m_χ) parameter space to be restricted by 3 sides or to be completely closed in case of the heavy mediator. In the case of the heavy mediator the stopping power is directly related to the dark matter mass and the heavier the mass the stronger the stopping power, hence the anti correlation between the critical cross section and the mass m_χ. In the case of the ultralight mediator, an inverse but much weaker relationship is visible.

The here presented analysis, a comparison between expectation and observation, resembles a very simple approach and does not allow for a complex inference. The lack of a background model makes any discovery impossible and only constraints can emerge from such an analysis. There is nothing inherently bad about this and a more complex analysis could quickly grow beyond the scope of a master thesis. The two different treatments of the "hot spot" results in almost the same exclusion bound and in the double logarithmic plot in figure 7.1, almost no difference is noticeable. Due to this, only the result from the spatial treatment of the "hot spot" is shown. The amount of useful data was unfortunately strongly reduced by the unstable trigger rate and the "hot spot", and in the end, the measurement time with the stable condition was shorter than a day. This made it impossible to utilize the previously mentioned modulation signature.

One could ask the question if the obtained results match the expectation of the project and to answer this question, it is useful to look at other experiments that searched for the same interactions. SENSEI, the silicon skipper-CCD experiment, has an interaction threshold that is roughly one magnitude lower than the threshold of xenon-based experiments and hence can probe masses about a order of magnitude smaller. The XENON experiments, which were conducted deep underground, reach much lower levels of backgrounds and consequently were sensitive to much lower interaction cross sections. Considering these features it seems reasonable that the exclusion region from Xurich II is placed somewhere between the two results. The location of Xurich II on the Earth's surface allows larger cross sections to be probed than by the XENON experiments, which seams accurately represented in the two figures above.

Xenon dual-phase TPCs are in general not designed for the search of very low energetic interactions and the main strengths for example the full event reconstruction are not possible if only the charge measurement is present. By how much this search technique can be adapted for such low energy signals, remains to be seen, but large improvements regarding single electron backgrounds have to be made before a discovery is even thinkable. An attempt to optimize the xenon dual-phase TPCs for the single to few electrons signal is done in a project called *Low Background Electron Counting Apparatus (LBECA)* [80] and the group hopes to improve upon the current exclusion bounds by a few orders of magnitude depending on the specific model. A new electrode design, a high work function material, and the usage of an additional silica cylinder within the TPC are believed to bring large improvements.

Interesting challenges also lie ahead for the development of even larger next-generation TPCs, of which one is currently being developed and tested at the University of Zurich [81]. Drifting electron over a much larger distance, with larger voltage biases and a higher xenon

purity are the challenges that are tried to be solved. The completely different approach with the Skipper-CCDs is an interesting alternative to the large-scale xenon experiments and it remains to be seen which technology becomes predominant in this particular field of dark matter search.

7.1 Closing Remarks

During the last year, that I was working on this project, I learned a lot about xenon TPCs, experimental physics, coding, and the life as a scientist in this field. The project was filled with challenges and often it was necessary to come up new solutions along the way. Working with data from an experiment that already had been conducted and put aside, required a lot of rethinking and reviewing, and the necessity to not only understand the experiment but also the theory made the work very interesting.

Personally I found the project a good learning experience because few unexpected events really enforced the rethinking of the search technique. For example the appearance of the "hot spot" or the unforeseen impact of the splitting algorithm where events, that showed the importance of the understanding of the experiment and its limits. On top of that comes the fact the unknown origin of the single electron signals caused the dark matter interpretation and so one could say that direct dark matter detection is in essence the study of detectors and backgrounds.

Towards the end of my thesis I was given the opportunity to present my work at the *International Conference on Topics in Astroparticle and Underground Physics 2021* (TAUP) and it was inspiring to see how new ideas are built on top of existing and how scientist push the limits further and further. At the conference I learned about new techniques [82, 83] and theories [84] that allow much smaller masses to be probed ($\sim$1 keV) and so it remains exciting to see if any of the new technologies can solve the riddle of dark matter.

Finally, I want to thank Professor Laura Baudis for the opportunity to work on this project and to be welcomed again after doing my bachelor thesis with XENON1T data. A very special thanks goes to Patricia Sanchez Lucas who was the absolute best support I could have wished for. Many times she found the time to sit down to discuss and debate things. Not only did she guide me through the project but also developed the data-driven approaches for the efficiencies. A big thanks also has to go to Giovanni Volta who was always there to discuss everyday-, coding- or physics problems.

Appendix A

Appendix

A.1 Implementation

Throughout the project *python* was used as the main coding language and in some instances, the ROOT framework was used through a python interface. The input/output was handled with a library called *uproot* and the main analysis was done using *awkward*-arrays, both tools are relatively young but incredibly useful. The *awkward-arrays* are very similar to the well-known *numpy*-arrays but allow arbitrary nested structures, which happened to appear all the time in this project. The packages are developed and maintained by the *Python in High Energy Physics* (PyHEP) group at CERN [85] and can highly be recommended.

A.2 Add-on Event Selection

If an S1-S2 event happens close to the cathode and the S1 is put in the middle of the waveform (trigger position) the remaining time to the end of the waveform does not have the length of one drift time Δt_{max}. The situation is illustrated in figure A.1. In this case, the waveform following the first one contains the small S2 and the veto time needs to extend into this waveform as well.

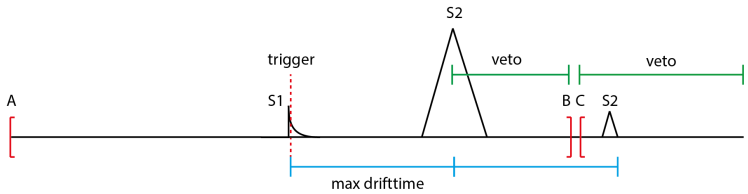

Figure A.1: Schematic event showing the time structure of an S1-S2 pair with maximal separation (maximal depth) and a small S2 following the large S2. The separation in time is represented to scale but the pulse shape and size are exaggerated. The first waveform is recorded between the marker A and B while the second waveform starts after the marker C.

To handle this case, the already discussed time vetos are enough, the first time veto starts at the large S2 and reaches until the end of the waveform (marker B) and the second veto removes Δt_{max} at the beginning of the following waveform (after marker C). This case is discussed here because initially it was believed that those events are quite abundant but an investigation showed that the noise cuts remove all most all waveforms with this structure. Initially, 9.2% of all the waveforms are close to each other (within 60 μs) and after the noise cuts only 0.72% of those waveforms remain.

A.3 Interaction with the Electric Dipole Moment

A dark matter interaction with the electric dipole moment would have the following form in the Lagrangian [86, 33].

$$\mathscr{L}_{\text{int}} \supset \frac{1}{\Lambda}\overline{\chi}\sigma^{\mu\nu}\gamma^5\chi F_{\mu\nu}\,, \quad \text{with } \sigma_{\mu\nu} = \frac{i}{2}[\gamma_\mu, \gamma_\nu]\,, \tag{A.1}$$

where Λ is the scale at which the electric dipole moment is generated. Although this interaction does not arise from the dark photon model, and the form factor cannot be derived from equation 3.1, the electric dipole interactions can easily be studied in the framework described in chapter 3 by setting the DM form factor to

$$F_{\text{DM}}(q) = \frac{q_{\text{ref}}}{q} \tag{A.2}$$

In figure A.2 the exclusion bounds for such an interaction are shown and no new parameter space can be excluded.

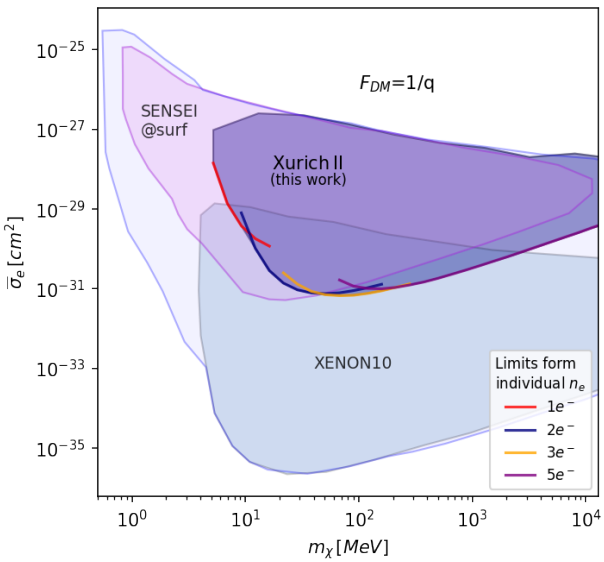

Figure A.2: Exclusion bounds for a dark matter interaction with the electric dipole moment. The current best (light blue area) are coming from XENON10 and SENSEI@surf and were taken from [31, 87, 33].

A.4 Precision Rate calculation

The rate calculation from section 3.1 was performed with the same code (wimprates) that was used in the S2-only analysis of XENON1T [54, 29] and since the initial calculation was done by Rouven Essig et al. [31] the question about the accuracy of the implementation naturally emerged. In figure A.3 a comparison between the used code and the original calculation is shown. The shape and accuracy of the implemented signal model are overall good but in the first bin, the implemented computation gives a 20-30% smaller rate than presented in the original work. This should not be a mayor problem because a smaller signal model will cause more conservative bounds.

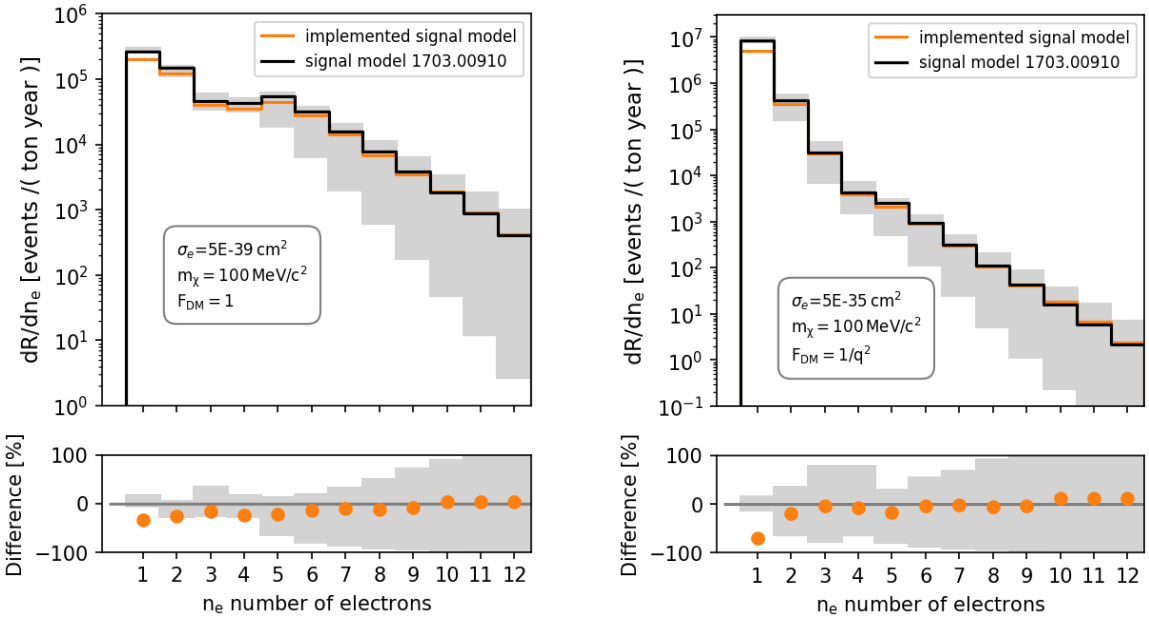

Figure A.3: In the upper panels two different signal models computed with the wimprates code (orange) are compared to the original rate (black) including the error bars of the original work (grey-band) arising from uncertainties in the secondary ionization. In the lower panels the relative differences are shown (orange dots) together with the residuals of the errors (grey band). The rate and the errors were copied from the original work, which introduces a small error which should not compromise the stated interpretation.

Bibliography

[1] F. Zwicky, *Die Rotverschiebung von extragalaktischen Nebeln*, *Helv. Phys. Acta* **6** (1933) 110.

[2] D. Clowe, A. Gonzalez and M. Markevitch, *Weak lensing mass reconstruction of the interacting cluster 1E0657-558: Direct evidence for the existence of dark matter*, *Astrophys. J.* **604** (2004) 596 [astro-ph/0312273].

[3] K. G. Begeman, A. H. Broeils and R. H. Sanders, *Extended rotation curves of spiral galaxies: dark halos and modified dynamics*, *Monthly Notices of the Royal Astronomical Society* **249** (1991) 523.

[4] V. C. Rubin and W. K. Ford, Jr., *Rotation of the Andromeda Nebula from a Spectroscopic Survey of Emission Regions*, *Astrophys. J.* **159** (1970) 379.

[5] V. Springel, C. S. Frenk and S. D. M. White, *The large-scale structure of the universe*, *Nature* **440** (2006) 1137.

[6] Planck collaboration, N. Aghanim et al., *Planck 2018 results. V. CMB power spectra and likelihoods*, *Astron. Astrophys.* **641** (2020) A5 [1907.12875].

[7] Planck collaboration, P. A. R. Ade et al., *Planck 2015 results. XV. Gravitational lensing*, *Astron. Astrophys.* **594** (2016) A15 [1502.01591].

[8] Planck collaboration, P. A. R. Ade et al., *Planck 2013 results. XV. CMB power spectra and likelihood*, *Astron. Astrophys.* **571** (2014) A15 [1303.5075].

[9] CMS collaboration, A. M. Sirunyan et al., *Search for dark matter produced with an energetic jet or a hadronically decaying W or Z boson at* $\sqrt{s} = 13$ *TeV*, *JHEP* **07** (2017) 014 [1703.01651].

[10] ATLAS collaboration, M. Aaboud et al., *Search for dark matter at* $\sqrt{s} = 13$ *TeV in final states containing an energetic photon and large missing transverse momentum with the ATLAS detector*, *Eur. Phys. J. C* **77** (2017) 393 [1704.03848].

[11] F. Kahlhoefer, *Review of LHC Dark Matter Searches*, *Int. J. Mod. Phys. A* **32** (2017) 1730006 [1702.02430].

[12] H.E.S.S. collaboration, H. Abdallah et al., *Search for dark matter signals towards a selection of recently detected DES dwarf galaxy satellites of the Milky Way with H.E.S.S.*, *Phys. Rev. D* **102** (2020) 062001 [2008.00688].

[13] CTA collaboration, H. Abdalla et al., *Sensitivity of the Cherenkov Telescope Array for probing cosmology and fundamental physics with gamma-ray propagation*, *JCAP* **02** (2021) 048 [2010.01349].

[14] Super-Kamiokande collaboration, S. Desai et al., *Search for dark matter WIMPs using upward through-going muons in Super-Kamiokande*, *Phys. Rev. D* **70** (2004) 083523 [hep-ex/0404025].

[15] IceCube collaboration, M. G. Aartsen et al., *First search for dark matter annihilations in the Earth with the IceCube Detector*, *Eur. Phys. J. C* **77** (2017) 82 [1609.01492].

[16] C. Thorpe-Morgan, D. Malyshev, C.-A. Stegen, A. Santangelo and J. Jochum, *Annihilating dark matter search with 12 yr of Fermi LAT data in nearby galaxy clusters*, *Mon. Not. Roy. Astron. Soc.* **502** (2021) 4039 [2010.11006].

[17] J. M. Gaskins, *A review of indirect searches for particle dark matter*, *Contemp. Phys.* **57** (2016) 496 [1604.00014].

[18] R. D. Peccei and H. R. Quinn, *Constraints Imposed by CP Conservation in the Presence of Instantons*, *Phys. Rev. D* **16** (1977) 1791.

[19] P. W. Graham, I. G. Irastorza, S. K. Lamoreaux, A. Lindner and K. A. van Bibber, *Experimental Searches for the Axion and Axion-Like Particles*, *Ann. Rev. Nucl. Part. Sci.* **65** (2015) 485 [1602.00039].

[20] L. Roszkowski, E. M. Sessolo and S. Trojanowski, *WIMP dark matter candidates and searches—current status and future prospects*, *Rept. Prog. Phys.* **81** (2018) 066201 [1707.06277].

[21] XENON collaboration, E. Aprile et al., *Dark Matter Search Results from a One Ton-Year Exposure of XENON1T*, *Phys. Rev. Lett.* **121** (2018) 111302 [1805.12562].

[22] LUX collaboration, D. S. Akerib et al., *Results from a search for dark matter in the complete LUX exposure*, *Phys. Rev. Lett.* **118** (2017) 021303 [1608.07648].

[23] PandaX-II collaboration, Q. Wang et al., *Results of dark matter search using the full PandaX-II exposure*, *Chin. Phys. C* **44** (2020) 125001 [2007.15469].

[24] DEAP collaboration, R. Ajaj et al., *Search for dark matter with a 231-day exposure of liquid argon using DEAP-3600 at SNOLAB*, *Phys. Rev. D* **100** (2019) 022004 [1902.04048].

[25] DarkSide collaboration, P. Agnes et al., *DarkSide-50 532-day Dark Matter Search with Low-Radioactivity Argon*, *Phys. Rev. D* **98** (2018) 102006 [1802.07198].

[26] J. Billard et al., *Direct Detection of Dark Matter – APPEC Committee Report*, 2104.07634.

[27] SENSEI collaboration, L. Barak et al., *SENSEI: Direct-Detection Results on sub-GeV Dark Matter from a New Skipper-CCD*, *Phys. Rev. Lett.* **125** (2020) 171802 [2004.11378].

[28] DAMIC collaboration, A. Aguilar-Arevalo et al., *Constraints on Light Dark Matter Particles Interacting with Electrons from DAMIC at SNOLAB*, *Phys. Rev. Lett.* **123** (2019) 181802 [1907.12628].

[29] XENON collaboration, E. Aprile et al., *Light Dark Matter Search with Ionization Signals in XENON1T*, *Phys. Rev. Lett.* **123** (2019) 251801 [1907.11485].

[30] R. Essig, A. Manalaysay, J. Mardon, P. Sorensen and T. Volansky, *First Direct Detection Limits on sub-GeV Dark Matter from XENON10*, *Phys. Rev. Lett.* **109** (2012) 021301 [1206.2644].

[31] R. Essig, T. Volansky and T.-T. Yu, *New Constraints and Prospects for sub-GeV Dark Matter Scattering off Electrons in Xenon*, *Phys. Rev. D* **96** (2017) 043017 [1703.00910].

[32] J. Rich, R. Rocchia and M. Spiro, *A Search for Strongly Interacting Dark Matter*, *Phys. Lett. B* **194** (1987) 173.

[33] T. Emken, R. Essig, C. Kouvaris and M. Sholapurkar, *Direct Detection of Strongly Interacting Sub-GeV Dark Matter via Electron Recoils*, *JCAP* **09** (2019) 070 [1905.06348].

[34] R. Essig, J. Mardon and T. Volansky, *Direct Detection of Sub-GeV Dark Matter*, *Phys. Rev. D* **85** (2012) 076007 [1108.5383].

[35] I. M. Bloch, A. Caputo, R. Essig, D. Redigolo, M. Sholapurkar and T. Volansky, *Exploring new physics with O(keV) electron recoils in direct detection experiments*, *JHEP* **01** (2021) 178 [2006.14521].

[36] L. Baudis, Y. Biondi, M. Galloway, F. Girard, S. Hochrein, S. Reichard et al., *The first dual-phase xenon TPC equipped with silicon photomultipliers and characterisation with ^{37}Ar*, *Eur. Phys. J. C* **80** (2020) 477 [2003.01731].

[37] SENSEI collaboration, O. Abramoff et al., *SENSEI: Direct-Detection Constraints on Sub-GeV Dark Matter from a Shallow Underground Run Using a Prototype Skipper-CCD*, *Phys. Rev. Lett.* **122** (2019) 161801 [1901.10478].

[38] A. Bolozdynya, *Two-phase emission detectors and their applications*, *Nuclear Instruments and Methods in Physics Research Section A: Accelerators, Spectrometers, Detectors and Associated Equipment* **422** (1999) 314.

[39] E. Aprile, J. Aalbers, F. Agostini, M. Alfonsi, F. D. Amaro, M. Anthony et al., *The xenon1t dark matter experiment*, *The European Physical Journal C* **77** (2017) .

[40] L. W. Goetzke, E. Aprile, M. Anthony, G. Plante and M. Weber, *Measurement of light and charge yield of low-energy electronic recoils in liquid xenon*, *Phys. Rev. D* **96** (2017) 103007 [1611.10322].

[41] XENON collaboration, E. Aprile et al., *Observation of two-neutrino double electron capture in ^{124}Xe with XENON1T*, *Nature* **568** (2019) 532 [1904.11002].

[42] EXO-200 collaboration, G. Anton et al., *Search for Neutrinoless Double-β Decay with the Complete EXO-200 Dataset*, *Phys. Rev. Lett.* **123** (2019) 161802 [1906.02723].

[43] L. Baudis, Y. Biondi, C. Capelli, M. Galloway, S. Kazama, A. Kish et al., *A Dual-phase Xenon TPC for Scintillation and Ionisation Yield Measurements in Liquid Xenon*, *Eur. Phys. J. C* **78** (2018) 351 [1712.08607].

[44] J. Cameron, J. Chen, B. Singh and N. Nica, *Nuclear data sheets for a = 37*, *Nuclear Data Sheets* **113** (2012) 365.

[45] V. I. B. et al., *Artificial Neutrino Source Based on the 37-Ar Isotope*, *Physics of Atomic Nuclei* **70** (2007) 300.

[46] L. W. Goetzke, E. Aprile, M. Anthony, G. Plante and M. Weber, *Measurement of light and charge yield of low-energy electronic recoils in liquid xenon*, *Phys. Rev. D* **96** (2017) 103007 [1611.10322].

[47] L. Baudis, P. Sanchez-Lucas and K. Thieme, *A measurement of the mean electronic excitation energy of liquid xenon*, 2109.07151.

[48] T. Emken and C. Kouvaris, *How blind are underground and surface detectors to strongly interacting Dark Matter?*, *Phys. Rev. D* **97** (2018) 115047 [1802.04764].

[49] T. Emken, C. Kouvaris and I. M. Shoemaker, *Terrestrial Effects on Dark Matter-Electron Scattering Experiments*, *Phys. Rev. D* **96** (2017) 015018 [1702.07750].

[50] S. K. Lee, M. Lisanti, S. Mishra-Sharma and B. R. Safdi, *Modulation Effects in Dark Matter-Electron Scattering Experiments*, *Phys. Rev. D* **92** (2015) 083517 [1508.07361].

[51] X. Chu, T. Hambye and M. H. G. Tytgat, *The Four Basic Ways of Creating Dark Matter Through a Portal*, *JCAP* **05** (2012) 034 [1112.0493].

[52] C. Dvorkin, T. Lin and K. Schutz, *Making dark matter out of light: Freeze-in from plasma effects*, *Physical Review D* **99** (2019) .

[53] P. Sorensen and C. E. Dahl, *Nuclear recoil energy scale in liquid xenon with application to the direct detection of dark matter*, *Phys. Rev. D* **83** (2011) 063501 [1101.6080].

[54] J. Aalbers, B. Pelssers and K. D. Mora, *wimprates: v0.3.0*, July, 2019. 10.5281/zenodo.3345959.

[55] T. Emken and C. Kouvaris, *DaMaSCUS-CRUST: Dark Matter Simulation Code for Underground Scatterings - Crust Edition*, Mar., 2018.

[56] G. Jungman, M. Kamionkowski and K. Griest, *Supersymmetric dark matter*, *Phys. Rept.* **267** (1996) 195 [hep-ph/9506380].

[57] M. C. Smith, G. R. Ruchti, A. Helmi, R. F. G. Wyse, J. P. Fulbright, K. C. Freeman et al., *The rave survey: constraining the local galactic escape speed*, *Monthly Notices of the Royal Astronomical Society* **379** (2007) 755.

[58] K. Freese, M. Lisanti and C. Savage, *Colloquium: Annual modulation of dark matter*, *Rev. Mod. Phys.* **85** (2013) 1561 [1209.3339].

[59] LUX collaboration, D. S. Akerib et al., *Investigation of background electron emission in the LUX detector*, *Phys. Rev. D* **102** (2020) 092004 [2004.07791].

[60] R. G. Wilson, *Vacuum thermionic work functions of polycrystalline be, ti, cr, fe, ni, cu, pt, and type 304 stainless steel*, *Journal of applied physics.* **37** (1966) .

[61] B. Edwards et al., *Measurement of single electron emission in two-phase xenon*, *Astropart. Phys.* **30** (2008) 54 [0708.0768].

[62] E. S. Chen, W. Wentworth and E. C. Chen, *The electron affinities of no and o2*, *Journal of Molecular Structure* **606** (2002) 1.

[63] J.-P. Schermann, *2 - Spectroscopy*. Elsevier, Amsterdam, 2008, https://doi.org/10.1016/B978-044452708-0.50003-4.

[64] J. Rienstra-Kiracofe, G. Tschumper, H. Schaefer, S. Nandi and G. Ellison, *Atomic and molecular electron affinities: Photoelectron experiments and theoretical computations*, *Chemical reviews* **102** (2002) 231.

[65] XENON100 collaboration, E. Aprile et al., *Observation and applications of single-electron charge signals in the XENON100 experiment*, *J. Phys. G* **41** (2014) 035201 [1311.1088].

[66] A. Kopec, A. L. Baxter, M. Clark, R. F. Lang, S. Li, J. Qin et al., *Correlated single- and few-electron backgrounds milliseconds after interactions in dual-phase liquid xenon time projection chambers*, *JINST* **16** (2021) P07014 [2103.05077].

[67] XENON10 collaboration, J. Angle et al., *A search for light dark matter in XENON10 data*, *Phys. Rev. Lett.* **107** (2011) 051301 [1104.3088].

[68] P. Sorensen, *Electron train backgrounds in liquid xenon dark matter search detectors are indeed due to thermalization and trapping*, 1702.04805.

[69] B. N. V. Edwards et al., *Extraction efficiency of drifting electrons in a two-phase xenon time projection chamber*, *JINST* **13** (2018) P01005 [1710.11032].

[70] J. Xu, S. Pereverzev, B. Lenardo, J. Kingston, D. Naim, A. Bernstein et al., *Electron extraction efficiency study for dual-phase xenon dark matter experiments*, *Phys. Rev. D* **99** (2019) 103024 [1904.02885].

[71] A. Bailey, *Dark matter searches and study of electrode design in LUX and LZ*, Ph.D. thesis, Imperial Coll., London, 8, 2016. 10.25560/41878.

[72] A. Tomás, H. M. Araújo, A. J. Bailey, A. Bayer, E. Chen, B. López Paredes et al., *Study and mitigation of spurious electron emission from cathodic wires in noble liquid time projection chambers*, *Astropart. Phys.* **103** (2018) 49 [1801.07231].

[73] R. H. Fowler and L. Nordheim, *Electron emission in intense electric fields*, *Proc. Roy. Soc. Lond. A* **119** (1928) 173.

[74] B. M. Cox and W. T. Williams, *Field-emission sites on unpolished stainless steel*, *Journal of Physics D: Applied Physics* **10** (1977) L5.

[75] ZEPLIN-III collaboration, E. Santos et al., *Single electron emission in two-phase xenon with application to the detection of coherent neutrino-nucleus scattering*, *JHEP* **12** (2011) 115 [1110.3056].

[76] XENON collaboration, E. Aprile et al., *Projected WIMP sensitivity of the XENONnT dark matter experiment*, *JCAP* **11** (2020) 031 [2007.08796].

[77] T. Doke and K. Masuda, *Present status of liquid rare gas scintillation detectors and their new application to gamma-ray calorimeters*, *Nucl. Instrum. Meth. A* **420** (1999) 62.

[78] Particle Data Group collaboration, M. Tanabashi et al., *Review of Particle Physics*, *Phys. Rev. D* **98** (2018) 030001.

[79] E. Bodnia et al., *The Electric Field Dependence of Single Electron Emission in the PIXeY Two-Phase Xenon Detector*, 2101.03686.

[80] A. Bernstein et al., *LBECA: A Low Background Electron Counting Apparatus for Sub-GeV Dark Matter Detection*, *J. Phys. Conf. Ser.* **1468** (2020) 012035 [2001.09311].

[81] L. Baudis, Y. Biondi, M. Galloway, F. Girard, A. Manfredini, N. McFadden et al., *Design and construction of Xenoscope – a full-scale vertical demonstrator for the DARWIN observatory*, *JINST* **16** (2021) P08052 [2105.13829].

[82] Y. Hochberg, I. Charaev, S.-W. Nam, V. Verma, M. Colangelo and K. K. Berggren, *Detecting Sub-GeV Dark Matter with Superconducting Nanowires*, *Phys. Rev. Lett.* **123** (2019) 151802 [1903.05101].

[83] Y. Hochberg, E. D. Kramer, N. Kurinsky and B. V. Lehmann, *Directional Detection of Light Dark Matter in Superconductors*, 2109.04473.

[84] Y. Hochberg, Y. Kahn, N. Kurinsky, B. V. Lehmann, T. C. Yu and K. K. Berggren, *Determining Dark Matter-Electron Scattering Rates from the Dielectric Function*, 2101.08263.

[85] J. Pivarski, P. Elmer and D. Lange, *Awkward Arrays in Python, C++, and Numba*, *EPJ Web Conf.* **245** (2020) 05023 [2001.06307].

[86] K. Sigurdson, M. Doran, A. Kurylov, R. R. Caldwell and M. Kamionkowski, *Dark-matter electric and magnetic dipole moments*, *Phys. Rev. D* **70** (2004) 083501 [astro-ph/0406355].

[87] SENSEI collaboration, M. Crisler, R. Essig, J. Estrada, G. Fernandez, J. Tiffenberg, M. Sofo haro et al., *SENSEI: First Direct-Detection Constraints on sub-GeV Dark Matter from a Surface Run*, *Phys. Rev. Lett.* **121** (2018) 061803 [1804.00088].